Anomalous relaxation and hyperuniform fluctuations in center-of-mass conserving systems with broken time-reversal symmetry

Anirban Mukherjee [1,2,*] Dhiraj Tapader,[1] Animesh Hazra [1,†] and Punyabrata Pradhan [1]

[1]*Department of Physics of Complex Systems, S. N. Bose National Centre for Basic Sciences, Block JD, Sector III, Salt Lake, Kolkata 700106, India*

[2]*Institute of Physics, Academia Sinica, Taipei 11529, Taiwan*

(Received 24 January 2024; revised 25 June 2024; accepted 9 July 2024; published 12 August 2024)

We study the Oslo model, a paradigm for absorbing-phase transition, on a one-dimensional ring of L sites with a fixed global density $\bar{\rho}$; we consider the system strictly above critical density ρ_c. Notably, microscopic dynamics conserve both mass and center of mass (CoM), but lack time-reversal symmetry. We show that, despite having highly constrained dynamics due to CoM conservation, the system exhibits diffusive relaxation away from criticality and superdiffusive relaxation near criticality. Furthermore, the CoM conservation severely restricts particle movement, causing the mobility—a transport coefficient analogous to the conductivity for charged particles—to vanish exactly. Indeed, the steady-state temporal growth of current fluctuation is qualitatively different from that observed in diffusive systems with a single conservation law. Remarkably, far from criticality where the relative density $\Delta = \bar{\rho} - \rho_c \gg \rho_c$, the second cumulant, or the variance, $\langle \mathcal{Q}_i^2(T, \Delta)\rangle_c$, of current $\mathcal{Q}_i$ across the ith bond up to time T in the steady-state saturates as $\langle \mathcal{Q}_i^2\rangle_c \simeq \Sigma_Q^2(\Delta) - \text{const}\, T^{-1/2}$; near criticality, it grows subdiffusively as $\langle \mathcal{Q}_i^2\rangle_c \sim T^{\alpha}$, with $0 < \alpha < 1/2$, and eventually saturates to $\Sigma_Q^2(\Delta)$. Interestingly, the asymptotic current fluctuation $\Sigma_Q^2(\Delta)$ is a nonmonotonic function of Δ: It diverges as $\Sigma_Q^2(\Delta) \sim \Delta^2$ for $\Delta \gg \rho_c$ and $\Sigma_Q^2(\Delta) \sim \Delta^{-\delta}$, with $\delta > 0$, for $\Delta \to 0^+$. Using a mass-conservation principle, we exactly determine the exponents $\delta = 2(1 - 1/\nu_\perp)/\nu_\perp$ and $\alpha = \delta/z\nu_\perp$ via the correlation-length and dynamic exponents, $\nu_\perp$ and z, respectively. Finally, we show that in the steady state the self-diffusion coefficient $\mathcal{D}_s(\bar{\rho})$ of tagged particles is connected to activity through the relation $\mathcal{D}_s(\bar{\rho}) = a(\bar{\rho})/\bar{\rho}$.

DOI: 10.1103/PhysRevE.110.024119

I. INTRODUCTION

A great deal of effort has been made in the literature on understanding large-scale properties of interacting many-body systems [1,2]. Indeed, a large-scale theory is typically formulated in terms of conservation laws [3–6] and requires only a few degrees of freedom, regardless of the systems' intrinsic microscopic dynamics, whether they are quantum, classical, or stochastic. While it is crucial, but perhaps relatively easy, to find the conserved densities, a rigorous microscopic derivation of hydrodynamics is a notoriously challenging task. This is primarily because, in most cases, one needs to compute the density-dependent transport coefficients when local stationary state is not known (or not even guaranteed); of course, the level of difficulty varies depending on the microscopic details one considers. In fact, stochastic dynamics are the simplest to deal with and have often been employed in the past to determine the role of conservation principles on relaxation and fluctuation characteristics of a system [7–9]. One may further inquire about the relevance of other principles, such as time-reversal symmetry and what happens near a critical point, among other things.

Recently there has been a surge of interest in characterizing large-scale transport in a variety of contexts, especially in quantum many-body systems like fractonic fluids [10–18], which, due to multiple conservation laws, possess a unique hydrodynamic structure. Indeed, by using a phenomenological theory, it was claimed that the time evolution of initially localized charge density in dipole-moment conserving systems, with short-ranged interaction, can only exhibit *subdiffusive* temporal growth [12,13,16,19]. Notably, the models investigated in these works have time-reversal symmetry present in the systems, and one might wonder what would happen if the time-reversal symmetry is broken. Of course, broken time-reversal symmetry allows for more choices in microscopic dynamics [20]; yet its role on the large-scale properties, particularly, of dipole-moment conserving systems, remains unknown. In this paper we provide a counterexample in terms of the paradigmatic Oslo model, which has both mass and center-of-mass (CoM) conservation (similar to dipole-moment conservation), but for which the time-reversal symmetry is broken and consequently subdiffusive time-evolution equation, such as Eq. (1) of Ref. [19], does not hold. Our findings demonstrate that the dynamic properties of CoM-conserving systems depend on microscopic details and need *not* always be subdiffusive.

Various conserved-mass transport processes, such as the random-organization model [21], chiral active matter [22,23], and a CoM-conserving variant of the Manna sandpile [20,24], among others [25], have been studied to better understand the role of CoM conservation in an out-of-equilibrium setting. For concreteness, in this work we focus on a minimal model system, i.e., the conserved-mass Oslo model [26,27],

*Contact author: anirban9973@gmail.com
†Contact author: animesh_edu@bose.res.in

which belongs to a broad class of threshold-activated transport processes, called conserved stochastic sandpiles [28]. The conserved Oslo model exhibits an absorbing phase transition [29,30], where the fraction $a(\rho)$ of *active* sites (those with mass greater than or equal to a threshold value) vanishes when density ρ falls below a critical value ρ_c. One of the most striking characteristics of such a transition is that, unlike in equilibrium, where fluctuations diverge for a continuous phase transition, mass fluctuations are suppressed further upon approaching criticality (from above) and, in the thermodynamic limit, eventually vanish at the critical point. Such a phenomenon is known as *hyperuniformity* [31–34] and has received significant attention [21,24,27,35–39].

While time series of dynamical activities (called "avalanches") in sandpiles have been extensively investigated [40–42], the time-dependent properties related to large-scale relaxation and transport have received much less attention [39,43–45]. Only recently has it been shown that the relaxation of long-wavelength density perturbations in the Manna sandpile, which has only one conserved quantity (mass), is diffusive far from criticality, but exhibits transport instabilities near criticality [46–48]. That is, the density-dependent transport coefficients—the self- and bulk-diffusion coefficients and the particle mobility—are all singular. Near criticality, while the mobility $\chi(\rho) \sim \Delta^{\beta}$ and the self-diffusion coefficient $\mathcal{D}_s(\rho) \sim \Delta^{\beta}$ vanish as a function of the relative density $\Delta = \rho - \rho_c$, the bulk-diffusion coefficient diverges $D(\rho) \sim \Delta^{-(1-\beta)}$; this results in anomalous (superdiffusive) transport where the dynamic exponent $z = 2 - (1-\beta)/\nu_\perp$ was found to be related to the (static) order parameter exponent β and correlation length exponent $\nu_\perp$ [46,47]. A detailed study of the near-critical properties of the conserved Oslo model was carried out in Ref. [27], and the standard critical exponents were numerically found to be close to the rational values with $\beta \approx 5/21$, $\nu_\perp \approx 4/3$, and $z \approx 10/7$. However, the question of how multiple conservation laws affect the dynamic properties, and the universality class [49,50], is not fully understood yet.

In this paper, by using a microscopic approach, we provide a large-scale characterization of various static and dynamic properties of mass and current in the Oslo model far from as well as near criticality (from above). We begin with long-wavelength density relaxations, demonstrating that, despite having highly constrained microscopic dynamics due to center-of-mass conservation, the Oslo model exhibits diffusive relaxation away from criticality and super-diffusive relaxation near criticality. Next we study dynamic fluctuations by analytically calculating unequal-time (two-point) correlation functions, and associated power spectra, involving current and mass. We find a mass-conservation principle, which connects (dynamic) current and (static) mass fluctuations, and exactly determine the decay exponents of the near-critical dynamic correlation functions in terms of the standard static exponents. Away from criticality, we exactly calculate within the closure scheme the decay exponent. Notably, the dynamic correlation functions are qualitatively different from that observed in diffusive systems with a single conservation law, and thus from that seen in the conserved Manna sandpiles. The findings are summarized below.

(1) *Density relaxation.* Far from (above) criticality, by performing a diffusive scaling of space $X \to x = X/L$, time $t \to \tau = t/L^2$, and local density $\rho(X,t) = g(X/L^2, t/L^2)$ with L being system size, we show that the space and time dependent coarse-grained density $g(x,\tau)$ satisfies a nonlinear diffusion equation $\partial_\tau g(x,\tau) = \partial_x[D(g)\partial_x g(x,\tau)]$, where $D(g) = da(g)/dg$ and $a(g)$ are the density-dependent bulk-diffusion coefficient and the steady-state activity, respectively. However, near (from above) criticality, the system becomes super-diffusive, with diverging $D \sim \Delta^{-(1-\beta)}$, thus implying relaxation time $\tau_r \sim L^2/D \sim L^z$ with the dynamic exponent $z = 2 - (1-\beta)/\nu_\perp$, a relation which is, quite remarkably, exactly satisfied by the critical exponents conjectured in Ref. [27].

(2) *A mass-conservation principle and its consequences.* We obtain a mass-conservation principle, which connects the the second cumulant, or the variance, $\langle \mathcal{Q}_i^2(T)\rangle_c$ of time-integrated bond-current and the (static) variance $\langle \Delta M_l^2\rangle$ of subsystem mass where $\Delta M_l = (M_l - \langle M_l\rangle)$, with $\mathcal{Q}_i(T)$ and M_l being the cumulative current across ith bond in a time interval $[0,T]$ and mass in a subsystem of size l, respectively. Indeed, for any fixed global density $\bar{\rho} > \rho_c$, the asymptotic values of current and mass fluctuations $\Sigma_Q^2(\bar{\rho}) = \lim_{L\to\infty}[\lim_{T\to\infty}\langle \mathcal{Q}_i^2(T)\rangle_c]$ and $\Sigma_M^2(\bar{\rho}) = \lim_{l\to\infty}[\lim_{L\to\infty}\langle \Delta M_l^2\rangle]$, respectively, converge to a finite value. By using the mass-conservation principle, they are related through an exact equality,

$$\Sigma_Q^2(\bar{\rho}) = \Sigma_M^2(\bar{\rho}). \tag{1}$$

Consequently, the particle mobility $\chi(\bar{\rho}) \equiv \lim_{L\to\infty}[\lim_{T\to\infty} L\langle \mathcal{Q}_i^2(T,L)\rangle_c/2T]$, which is defined by taking the infinite-time limit first and then the infinite-volume limit, vanishes identically for any (global) density $\bar{\rho} > \rho_c$, as opposed to the conserved Manna sandpile, or any other diffusive systems with a single conservation law, for which the mobility is finite (except at critical point). Interestingly, both the asymptotic current and mass fluctuations, $\Sigma_Q^2(\bar{\rho})$ and $\Sigma_M^2(\bar{\rho})$, respectively, are a nonmonotonic function of density; as a function of $\Delta = \bar{\rho} - \rho_c$, they diverge as Δ^2 for $\Delta \gg \rho_c$ and as $\Delta^{-\delta}$, with $\delta > 0$, for $\Delta \to 0^+$.

(3) *Finite-time characteristics of time-integrated bond current.* Temporal growth of time-integrated current fluctuation is qualitatively different from that in diffusive systems with a single conservation law. In the regime $1 \ll T \ll L^2$, we show that, far from criticality, the time-integrated bond-current fluctuation saturates as $\langle \mathcal{Q}_i^2(T)\rangle_c \simeq \Sigma_Q^2(\bar{\rho}) - \text{const}\, T^{-1/2}$. However, near criticality, the current fluctuation grows as $\langle \mathcal{Q}_i^2(T)\rangle_c \sim T^{\alpha}$, but eventually saturates to a large $\Sigma_Q^2(\bar{\rho}) \sim \Delta^{-\delta}$. By using Eq. (1), we determine $\alpha = \delta/\nu_\perp z$ and $\delta = 2\zeta/\nu_\perp = 2(1 - 1/\nu_\perp)/\nu_\perp$ in terms of the standard critical exponents: hyperuniformity, correlation length, and dynamic exponents ζ, $\nu_\perp$, and z, respectively.

(4) *Statistics of instantaneous current.* By decomposing instantaneous current $\mathcal{J}_i(t) \equiv d\mathcal{Q}_i(t)/dt$ as a sum of diffusive part $\mathcal{J}^{(d)}$ and a fluctuating (or "noise") part $\mathcal{J}^{(fl)}$, i.e., $\mathcal{J}_i(t) = \mathcal{J}^{(d)}(t) + \mathcal{J}^{(fl)}(t)$, we calculate respective dynamic correlation functions. We show that, far from criticality and for long times t, the current correlation function is long-ranged and decays as $\langle \mathcal{J}_i(t)\mathcal{J}_i(0)\rangle \simeq -\text{const}\, t^{-5/2}$, which is faster than

that in the Manna sandpile, having a $t^{-3/2}$ power-law decay. However, the correlation function for the fluctuating current is delta correlated in time, i.e., $\langle \mathcal{J}_r^{(fl)}(t)\mathcal{J}_0^{(fl)}(0)\rangle_c = \Gamma_r(\bar{\rho})\delta(t)$, with space-integrated strength $\sum \Gamma_r = 0$, resulting due to the CoM conservation and thus implying greatly suppressed current fluctuations and spatial and temporal hyperuniformity (sometimes of an extreme form) in the system.

(5) *Power spectrum of current and mass.* In the small-frequency limit $f \to 0$, we find that the power spectrum of bond current $S_{\mathcal{J}}(f) \sim f^{\psi_{\mathcal{J}}}$ with $\psi_{\mathcal{J}} = 1/2 + \mu$, where $\mu = 1$ away from criticality and $\mu = 1/2 - \delta/\nu_\perp z$ near criticality; indeed, the decay is much faster compared to diffusive systems with a single conservation law, where $\mu = 0$. Notably, these findings imply that the current fluctuation far from criticality is much more suppressed than that near criticality. On the other hand, for small frequencies, the power spectrum $S_M(f) \sim f^{-\psi_M}$ for subsystem mass grows with decreasing frequency, where exponent is $\psi_M = 2 - \psi_{\mathcal{J}}$; similar to the current fluctuations, the mass fluctuations far from criticality are much more suppressed than that near criticality.

(6) *Static structure factor.* We find that the static subsystem mass fluctuations are always hyperuniform, both far from and near criticality (strictly, from above), where the structure factor $S(q) \sim q^{\gamma}$ with $\gamma > 2$. Far from criticality, we analytically calculate, within our closure scheme, the structure factor and show that, for small wave number $q \to 0$, the exponent $\gamma = 2$, exhibiting an extreme form of ("class I") hyperuniformity [32] in the "active" phase and thus providing a microscopic explanation for previous numerical observations in a CoM-conserving system [24]. Notably, the mass fluctuation is more suppressed far from criticality than that near criticality, consistent with the dynamic behavior of current and mass fluctuations [as described in points (II)–(V)].

(7) *Self-diffusion coefficient of tagged particles.* Finally, we show that the density-dependent self-diffusion coefficient $\mathcal{D}_s$ exactly equals the ratio of density-dependent activity to the density itself, i.e., $\mathcal{D}_s(\bar{\rho}) = a(\bar{\rho})/\bar{\rho}$. The result implies that, like conserved Manna sandpile [44,48], the behavior of the self-diffusion coefficient near criticality is exactly same as that of the order parameter, the density-dependent activity. That is, like the activity, $\mathcal{D}_s(\Delta)$ decays as Δ^{β}, where β is the order-parameter exponent.

Note that, on a periodic domain, average current is zero in the steady state (e.g., $\langle \mathcal{Q}_i(T)\rangle = 0$) and, throughout the paper, we write the second cumulant, or the variance, of current in terms of the second moment [e.g., $\langle \mathcal{Q}_i^2(T)\rangle_c = \langle \mathcal{Q}_i^2(T)\rangle$].

We organize the paper as follows. In Sec. II we define the Oslo model, and in Sec. III A we derive hydrodynamics of the model. Then in Sec. III B we compare our hydrodynamic theory with simulations for both far-from and near-critical density regimes. We describe the calculation of the current correlation in Sec. IV A 2 and obtain general unequal-space and unequal-time integrated current fluctuations. Similarly in Sec. IV B we calculate the dynamic correlations involving mass and obtain a fluctuation relation. In Sec. IV C we compare our theoretical results for dynamic fluctuations with the simulations. In Secs. IV C 5 and IV B we theoretically obtain and check the power spectra of current and mass. We calculate the self-diffusion coefficient of the Oslo model in Sec. VI, and in Sec. V we calculate the static structure factor. Finally, we conclude with a summary in Sec. VII.

II. MODEL

In this section we consider the paradigmatic Oslo model, which is an example of threshold-activated systems, collectively called "sandpiles" [51], and was introduced to understand certain scale-invariant features observed in granular piles [26]. Dynamical activities in these highly nonlinear systems propagate in space and time via intermittent burstlike "avalanches," resulting in long-ranged spatiotemporal correlations. Sandpiles have several variants, depending on whether mass variable being discrete or continuous, particle-transfer rules being deterministic or stochastic [52–55], randomness in threshold mass [26], "stickiness" [56,57], and various other local and nonlocal variations of microscopic dynamics [58].

We define the conserved-mass Oslo model—a prototype of conserved stochastic sandpiles [55]—on a one-dimensional periodic lattice of size L. The continuous-time microscopic dynamical rule for a site $i \in [0, 1, 2, \ldots, L-1]$ is specified in terms of two local dynamical variables: the mass and the threshold mass for toppling. Mass (also called "height") or number of particles $m_i \geqslant 0$ at site i takes integer values with total mass $N = \sum_{i=0}^{L-1} m_i$ being conserved; the global density is denoted as $\bar{\rho} = N/L$. The threshold value $m_{c,i}$ of mass at site i, with $m_{c,i} = 2$ or 3, is reset to a new random value after a toppling occurs at the site. An *active* site i, with $m_i \geqslant m_{c,i}$, topples with unit rate by *deterministically* transferring two particles, one to its right-nearest neighbor and another to its left-nearest neighbor, followed by a random resetting of the threshold mass at site i. The Oslo model is a stochastic variant of the BTW sandpile [51] in that the threshold mass can take random values; furthermore, the CoM remains conserved in both the Oslo and BTW models due to the deterministic mass transfer: That is, a two-particle transfer rule is implemented where one particle goes to the right and the other goes to the left. However, the Oslo model should be contrasted with the Manna sandpile [54], which has a fixed threshold value (like the BTW sandpile), a stochastic particle-transfer rule (two particles transferred independently, each going to the right or left with probability 1/2) and thus *no* CoM conservation.

We write below, for the conserved-mass Oslo model, continuous-time update rules of local mass $m_i(t)$ in an infinitesimal time interval $(t, t+dt)$:

$$m_i(t+dt) = \begin{cases} \text{events} & \text{probabilities} \\ m_i(t)+1 & \hat{a}_{i+1}dt \\ m_i(t)+1 & \hat{a}_{i-1}dt \\ m_i(t)-2 & \hat{a}_i dt \\ m_i(t) & (1-\Sigma dt), \end{cases} \tag{2}$$

where the sum of (exit) rates $\Sigma = (\hat{a}_{i+1} + \hat{a}_{i-1} + \hat{a}_i)$, and we denote $\hat{a}_i$ as an indicator function,

$$\hat{a}_i = \begin{cases} 1 & \text{for } m_i \geqslant m_{c,i}, \\ 0 & \text{otherwise.} \end{cases} \tag{3}$$

Clearly, the system violates detailed balance (or, the microcopic time reversibility) in the bulk as the reverse transition corresponding to any allowed transition is forbidden. The system exhibits a continuous absorbing-phase transition (APT)

below a critical density $\rho_c \approx 1.732594$ [27]. That is, for global density $\bar{\rho} < \rho_c$, dynamical activities (topplings) cease to exist, and the system settles into one of the many absorbing states with the number of active sites being zero and the system being completely frozen in time. On the other hand, for $\bar{\rho} > \rho_c$, the system remains in an active state, where the dynamical activities go on forever. The absorbing phase transition is characterized through the steady-state density of active sites or simply called activity $a(\bar{\rho})$, the "order parameter" of the system, which is computed as the steady-state average $a(\bar{\rho}) = \sum_i \langle \hat{a}_i \rangle / L$ and depends on the global density $\bar{\rho}$. Interestingly, the standard critical exponents for the Oslo model are known through large-scale simulations and *close to rational fractions*, i.e., the order-parameter, correlation length, and dynamic exponents are given by $\beta \approx 5/21$, $\nu_\perp \approx 4/3$, and $z \approx 10/7$, respectively [27].

III. THEORY OF DENSITY RELAXATION

A. Hydrodynamics

In this section we first derive an exact hydrodynamic structure of the Oslo model. While, for the Manna sandpile, the stochastic nature of particle transfer ensures diffusive relaxation (far from criticality) [46,47], it is not quite evident that the density relaxation in the Oslo model will be diffusive as well. Indeed, for relaxation processes in the far-from-critical regime, we provide below a precise theoretical argument for why the relaxation process in the latter case is in fact diffusive. We also argue why a suitably coarse-grained density field must satisfy a nonlinear diffusion equation, quite similar to that arises in the case of the Manna sandpile [46,47].

Below we consider the Oslo model on a one-dimensional periodic lattice having L sites. We specify the system through a local density $\rho_X(t) = \langle m_X(t) \rangle$, the average of the particle number $m_X(t)$ at site X and time t; or, equivalently, we can define a local excess (or, relative) density $\Delta(X,t) = (\rho_X(t) - \rho_c)$. By using the microscopic dynamics of Eq. (2), we can derive the density-evolution equation,

$$\frac{\partial \rho_X(t)}{\partial t} = [a_{X-1}(t) - 2a_X(t) + a_{X+1}(t)] \equiv \nabla^2 [a_X(t)], \quad (4)$$

where $a_X(t)$ is the space- and time-dependent average local activity; here we denote ∇^2 as the discrete Laplacian. It is worth noting here that the density-evolution equation for the Oslo model is exactly the same in terms of appropriately defined local activity [46]. Then we immediately find that the above equation for locally conserved density field can be expressed as a (discrete-space) continuity equation $\partial \rho_X(t)/\partial t = J(X,t) - J(X+1,t)$, where we define a local current

$$J(X,t) = a_{X-1}(t) - a_X(t) \equiv -\nabla a_X(t); \quad (5)$$

note that we have the local current manifestly expressed as a negative of the (discrete) gradient of activity $a_X(t)$, which can be readily recognized as diffusive current satisfying the Fick's law. Importantly, we now invoke a local-equilibrium-like ("local-steady-state") property of the inhomogeneous state so that the ("locally steady") activity at long times can essentially be determined by the local-steady-state activity, which depends on the local coarse-grained density, being the slow variable in the system. In other words, we write $a_X(t) = \langle \hat{a}_X \rangle^{st}_{\rho(X,t)} = a[\rho_X(t)]$, where $\langle . \rangle^{st}_{\rho_X(t)}$ represents the steady-state average conditioned on the fact that the local density is $\rho_X(t)$. As a result, the density evolution can be written in terms of a *nonlinear* diffusion equation,

$$\frac{\partial \rho_X(t)}{\partial t} \simeq \frac{\partial^2 a[\rho_X(t)]}{\partial X^2} = -\frac{\partial J(\rho_X)}{\partial X}. \quad (6)$$

In the above equation, $a(\rho)$ is the activity calculated, in the steady state, as a function of density ρ. Now, the diffusive current can be immediately identified as $J(\rho) = -D(\rho)\partial\rho/\partial X$, where the density-dependent bulk-diffusion coefficient is written as the derivative of (density-dependent) steady-state activity w.r.t. density,

$$D(\rho) = \frac{da(\rho)}{d\rho}. \quad (7)$$

The manifestly diffusive structure of Eq. (6) allows us to write the space- and time-dependent density in the scaling form as

$$\rho_X(t) = g\left(\frac{X}{L}, \frac{t}{L^2}\right), \quad (8)$$

which, as one can immediately show, satisfies a nonlinear diffusion equation for coarse-grained density field $g(x,\tau)$,

$$\frac{\partial g(x,\tau)}{\partial \tau} = \frac{\partial^2 a(g)}{\partial x^2}. \quad (9)$$

Note that, in the limit of L large, the rescaled space x and time τ in the above equation can be considered a continuous variable, and the local coarse-grained activity $a(g)$ is a nonlinear function of g. In other words, the local-equilibrium (or, local-steady-state) hypothesis used to derive Eq. (9) translates into the assertion that the local activity is indeed slave to local density. Furthermore, on a large (coarse-grained) spatial scale, we can represent the initial density as a function of scaled position $x = X/L$, i.e., $\rho(X, t=0) \equiv \rho_{\rm in}(X) = g_{\rm in}(X/L)$. Clearly, the above equation must be solved given the initial condition $g(x, \tau = 0) = g_{\rm in}(x)$ and has a unique solution. Now, with a given density field, the CoM is also fixed locally (as well as globally) and does not constitute an independent equation for the other locally conserved quantity, i.e., the local CoM field.

It is quite expected that, far from criticality, correlation length ξ in the system should be finite, and hence the bulk-diffusion coefficient, as we find in this study, is nonzero and finite. In such a scenario, the density perturbations, characterized by wave numbers $k \to 0$ being small, relax over a timescale $1/k^2 D(\rho)$; equivalently, for a system with size L, we have the relaxation time $\tau_r \sim L^2/D(\rho)$. The above mentioned argument for diffusive scaling, on the other hand, does not work in the near-critical regime. In fact, for near-critical density $\rho_X(t) \sim \rho_c^+$, the bulk-diffusion coefficient diverges as $D(\rho) \sim (\rho - \rho_c)^{\beta-1}$ because, in this scaling regime, the activity $a(\rho) \sim (\rho - \rho_c)^\beta$ has a form of a power law with order-parameter exponent β, which, though being model-dependent, is usually less than one [27,55]; in other words, the particle transport should be anomalous (superdiffusive) near criticality (strictly, from above).

Therefore we conclude that the hydrodynamic mechanism for density relaxation in the conserved Oslo model is indeed quite similar to that in the case of the conserved Manna sandpile. This particular finding establishes one of the main results

of this paper that, despite constrained dynamics [19,20], the density relaxation is *not always subdiffusive* in systems with CoM conservation. However, we must mention here that, due to the CoM conservation, the dynamic correlation functions for density and current, on the contrary, are drastically different from that observed in the Manna sandpile [48].

In the subsequent section, we obtain explicit theoretical solutions of Eq. (9) (mostly obtained by a numerical integration scheme) for various initial conditions and compare them with direct Monte Carlo simulations. For the purpose of comparing the results for the Oslo model with that in the Manna sandpile, we consider similar parameter regimes (e.g., for densities and system sizes, etc.) and the initial conditions (e.g., steplike, wedgelike, and Gaussian density profiles) as considered previously [47].

B. Comparison: Theory and simulations

In this section we explicitly obtain the solutions of the nonlinear diffusion equation (9), corresponding to various initial conditions $\rho(x,0) \equiv g_{\rm in}(x)$ in the domain $x \in [0,1]$; we consider throughout a periodic boundary condition $\rho(0) = \rho(1)$. Starting from an initial density profile, we study the relaxation of density profiles on macroscopically large spatiotemporal scales. These initial density profiles, in most cases, are taken as a step, or box, density profile; though, in a few cases, wedge and Gaussian initial density profiles are also considered. In this way, we verify the nonlinear diffusion equation (9), where we perform microscopic simulations in various density regimes (far from and near criticality) and compare the space- and time-dependent density with that obtained by solving Eq. (9).

To investigate the hydrodynamic theory, we numerically integrate Eq. (9) by using the Euler method where we discretize space x as $\delta x = 10^{-3}$ and time τ as $\delta\tau = 10^{-7}$, respectively. We integrate the diffusion equation by using the explicit density dependence of the nonlinear function $a(\rho)$, the steady-state activity. We generate the steady-state activity $a(\rho)$ vs ρ from direct microscopic simulations of the Oslo model and measure the activity in steps of density $\delta\rho = 10^{-2}$. In the numerical integration scheme, we calculate $a(\rho)$, by performing linear interpolation for densities having values smaller than the least possible value of density, i.e., for density values in the range $[\rho, \rho + \delta\rho]$.

1. Relaxation of density profile far from criticality

In this section, we study the density relaxation when the system is far from the criticality. To produce a specified initial density profile in simulations, we have generated numerous random initial configurations and done an ensemble average over them. To observe the density profile at subsequent times, we evolve the initial density profile through the microscopic stochastic dynamics up to those times; we then average over the random initial configurations as well as stochastic trajectories.

Relaxation of step initial profile. First, we study the far-from-critical regime, where we consider the relaxation of a step initial density profile, which spreads on an infinite domain having a density above the critical density. We take the step initial profile having height ρ_1 over a uniform density $\rho_0 > \rho_c$ of the background. We are interested in characterizing how this initial step density perturbation relaxes around the origin $X = 0$. To study this, we take an initial density profile having the form

$$\rho_{\rm in}(X) = \begin{cases} \rho_1 + \rho_0 & \text{for } -\infty < X \leqslant 0, \\ \rho_0 & \text{otherwise.} \end{cases} \tag{10}$$

Here $\rho_1 = 1.2$ is the height of the step, which is constructed over a uniform background density $\rho_0 = 1.8$ on the right half of the origin. We start with the following scaling ansatz where the (shifted) density profile:

$$\rho_x(t) - \rho_0 = \mathcal{Y}\left(\frac{X}{\sqrt{t}}\right), \tag{11}$$

is written as a function of a scaling variable $X/\sqrt{t}$. Now, by substituting the above ansatz in Eq. (6), one can show that the scaling function $\mathcal{Y}(z)$, with the scaling variable $z = X/t^{1/2}$, satisfies the following equation involving only a single variable z [instead of two variables X and t in Eq. (6)]:

$$-z\frac{d\mathcal{Y}(z)}{dz} = 2\frac{d}{dz}\left[\mathcal{D}(\mathcal{Y})\frac{d\mathcal{Y}}{dz}\right], \tag{12}$$

which should be solved with the boundary conditions $\mathcal{Y}(-\infty) = \rho_1$ and $\mathcal{Y}(\infty) = 0$. Of course, to find $\mathcal{Y}(z)$ analytically as an explicit function of z, we need to determine the functional form of $\mathcal{D}(\mathcal{Y}) = D(\rho_0 + \mathcal{Y})$, which is not known analytically for the Oslo model. However, $\mathcal{D}(\mathcal{Y})$ can be calculated numerically using Eq. (7), where steady-state activity $a(\rho)$ as a function of density ρ is directly calculated from Monte Carlo simulations. Now, Eq. (12) can be solved through numerical integration and the scaling function $\mathcal{Y}(z)$ is plotted as a function of z in Fig. 1 (solid red line). Remarkably, our theory and simulations are in excellent agreement with each other, demonstrating that the far-from-critical relaxations are indeed governed by a *nonlinear* diffusion equation (9), where the bulk-diffusion coefficient is density-dependent.

In Fig. 1 the relaxation of step initial density profile (10) over an infinite domain is plotted and how this profile spread over the right half of the origin is studied. The global density of the system is taken $\bar{\rho} = 2.4$, which is far away from criticality. So it can be assumed that the transport of particles on the lattice will be diffusive resulting in a finite coefficient of diffusion of the system. We plot the shifted density profile $\rho(X,t) - \rho_0$ vs position X in of Fig. 1(a) for (Monte Carlo) times $t = 2 \times 10^3$ (magenta asterisks), 5×10^3 (yellow open squares), 10^4 (blue filled squares), 2×10^4 (red open circles), and 4×10^4 (black filled circles). In Fig. 1(b) we depict the scaling function of the shifted density profile as a function of the scaling variable z. The red solid line is obtained from the numerical solution of Eq. (12), and it matches quite well with the simulation results, indicated by the data points in the plot. We verify the density profiles obtained from microscopic simulation with the profiles from hydrodynamic equation (6). We find that profiles from simulation (points) and hydrodynamic (lines) theory agree well. Just to check the effect of nonlinearity, we also compare the actual solution $\mathcal{Y}(z)$ with the solution of Eq. (12) with an effective (constant) bulk-diffusion coefficient $D_{\rm eff} = D(\rho_{\rm eff})$ where $\rho_{\rm eff} = \rho_0 + \rho_1/2$; one could see that the effective (constant D) solution

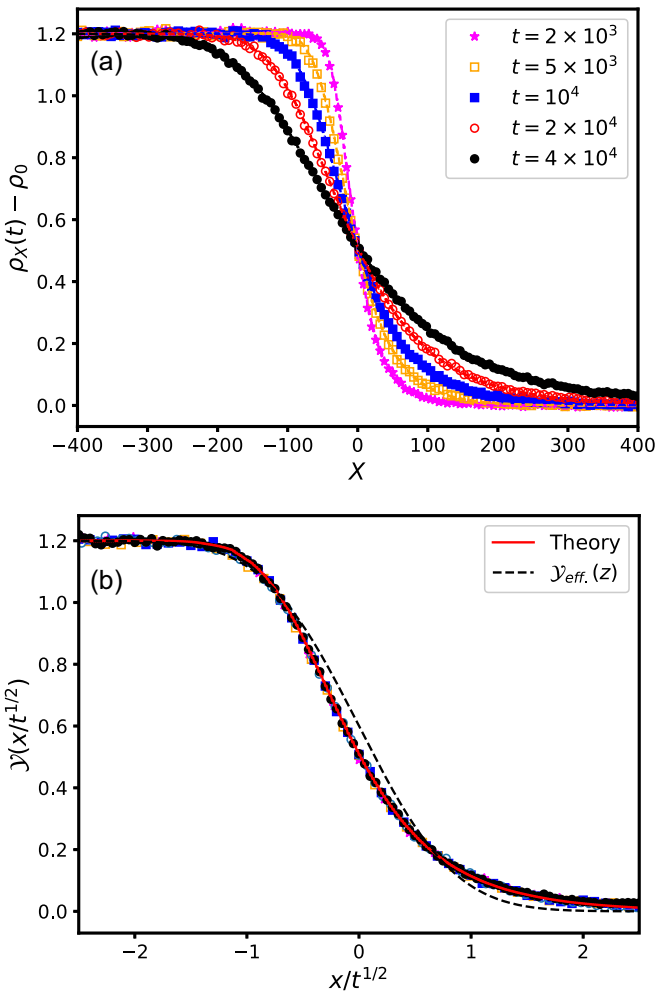

FIG. 1. Relaxation of a steplike density profile far from criticality on infinite domain. (a) Excess density over the uniform background density $\rho_x(t) - \rho_0$ for a step initial profile (10) is plotted vs position X. The background density is taken $\rho_0 = 1.8 > \rho_c$ and the height of the step on the left half of origin $\rho_1 = 1.2$. (b) We plot the shifted density profile $\mathcal{Y}(z)$ vs scaling variable $z = X/t^{1/2}$. Red solid line represents the theoretical line obtained from the numerical solution of nonlinear Eq. (12), and black dashed line represents the solution of the corresponding linear equation with a constant effective diffusivity (comparison purpose). For both panels, this step profile on the right half evolves and spreads over the domain; the profiles for different Monte Carlo times $t = 2.0 \times 10^3$ (magenta asterisks), 5.0×10^3 (orange open squares), 10^4 (blue filled squares), 2.0×10^4 (red open circles), and 4.0×10^4 (black filled circles) are plotted. System size $L = 2000$ and global density $\bar{\rho} = 2.4$. Lines: hydrodynamic; points: simulation.

$\mathcal{Y}_{\text{eff}}(z) = \rho_1/2 + \rho_1 \text{erf}(-z/\sqrt{4D_{\text{eff}}})/2$, which is plotted in the same figure (dashed black line).

Verification of diffusive scaling limit. The diffusive scaling limit used to arrive at Eq. (9) from Eq. (6) is verified in this section. To check the scaling, we need to produce a scaled density profile $\rho(X = xL, t = \tau L^2) \equiv g(x, \tau)$, which is a function of scaled position $x = X/L^2$ for different system sizes and for different times, by keeping hydrodynamic time $\tau = t/L^2$ fixed. So, according to the assertion that there exists a diffusive scaling limit, the density profiles for different system sizes and different times must collapse onto each other; moreover, the collapsed profile must also be described by the nonlinear diffusion equation (9).

Now to check the above mentioned scaling collapse in simulations, we take two different initial density profiles having a wedge and two steps (box). We take the following steplike initial density profile $g_{\text{in}}(x) \equiv \rho(x, \tau = 0)$:

$$g_{\text{in}}(x) = \begin{cases} \rho_1 + \rho_0 & \text{for } x_1 < x < x_2, \\ \rho_0 & \text{otherwise,} \end{cases} \tag{13}$$

where $\rho_1 = 7.0$ is the height of the step between the regions $x_1 = 3/8$ and $x_2 = 5/8$, over a uniform background density $\rho_0 = 1.8$, maintaining the global density $\bar{\rho} = 3.55$. The wedgelike initial profile is given by

$$g_{\text{in}}(x) = \begin{cases} \rho_0 + 2\rho_1(x - x_1)/w & \text{for } x_1 < x < x_2, \\ \rho_0 + 2\rho_1(x_3 - x)/w & \text{for } x_2 < x < x_3, \\ \rho_0 & \text{otherwise.} \end{cases} \tag{14}$$

We create the above wedgelike initial density profile by distributing $N_1 = L(\bar{\rho} - \rho_0)$ particles by keeping the center of the wedge at $x_2 = 1/2$. The width of the profile is taken to be $w = 1/2$, from position $x_1 = (1 - w)/2$ to $x_3 = (1 + w)/2$. The height is taken to be $\rho_1 = 1.75$, placed over a background density $\rho_0 = 1.8$, chosen to be away from critical density ρ_c. In both of the cases, the global density is kept fixed at $\bar{\rho} = 3.55$. For both the initial conditions, we check the diffusive scaling limit for system sizes $L = 200$, 400, 600, and 1000.

We present in Fig. 2 the scaled density profile $g(x, \tau) - \bar{\rho}$ over the global density as a function of scaled position $x = X/L$. We generate the profiles for a fixed hydrodynamic time $\tau = 0.5$, i.e., we have allowed the systems to evolve up to a Monte Carlo time $t = \tau L^2$ for respective system sizes. In simulations, with step initial profile presented in Fig. 2(a) and for wedgelike initial profile presented in Fig. 2(b), we evolve the density profiles up to times $t = 2 \times 10^4$ where $L = 200$ (pink squares), $t = 8 \times 10^4$ where $L = 400$ (black circles), $t = 1.8 \times 10^5$ where $L = 600$ (green asterisks), and $t = 5 \times 10^5$ where $L = 1000$ (blue triangles). We observe that all these density profiles collapse on to each other quite well. On the other hand, we obtain the scaled density function $g(x, \tau = 0.5)$ by numerically integrating the hydrodynamic equation (9) up to the hydrodynamic time $\tau = 0.5$ for both initial conditions. From Fig. 2 we find that the scaled density profile obtained from hydrodynamic theory and the collapsed density profiles obtained using simulations are in very good agreement.

2. *Near-critical density relaxation*

The near-critical regime corresponds to local excess density $\Delta(X, t) \sim L^{-1/\nu_\perp}$, where the local excess density is very small; so the correlation length is large and it is of the order of the system size. As the correlation length is large, the transport is *not* diffusive anymore. This is because the activity field $a(\rho) \sim \Delta^\beta$ has a form of a power law where we have exponent $\beta < 1$ and thus a singularity at the critical point $\rho = \rho_c$. As a result, the bulk-diffusion coefficient, which is simply the derivative of the activity with respect to density, varies as $D(\Delta) \sim \Delta^{-(1-\beta)}$, which diverges at the critical point. In the

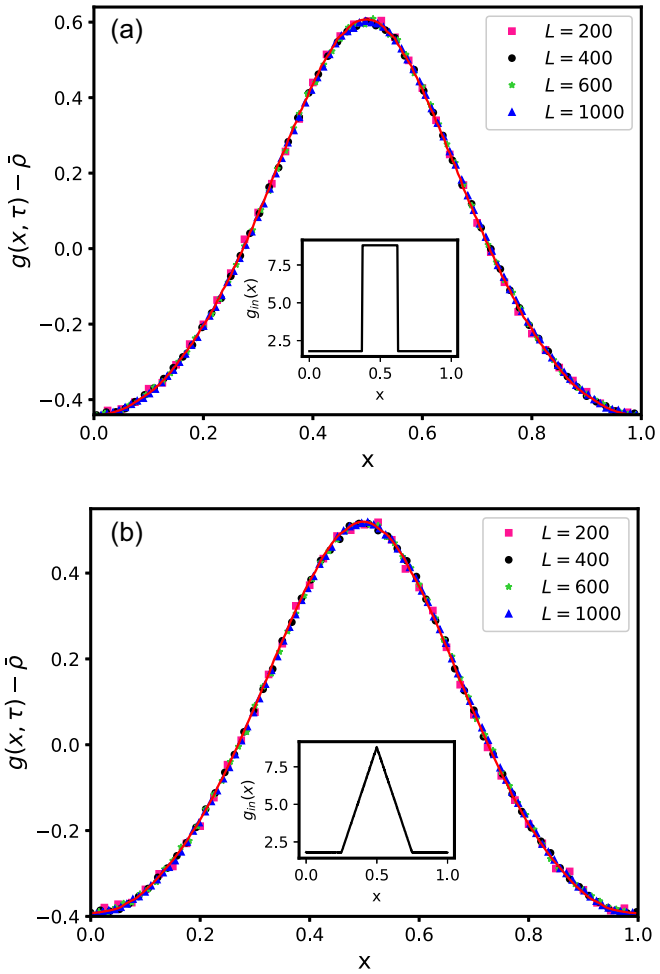

FIG. 2. Verification of diffusive scaling limit in far-from-critical regime. Scaled density profile $g(x,\tau) - \bar{\rho}$ vs rescaled position $x = X/L$ are plotted at times $t = 2.0 \times 10^4$ for $L = 200$ (pink squares), $t = 8.0 \times 10^4$ for $L = 400$ (black), $t = 1.8 \times 10^5$ for $L = 600$ (green asterisks), and $t = 5.0 \times 10^5$ for $L = 1000$ (blue), where the hydrodynamic time is kept fixed at $\tau = t/L^2 = 0.5$. Simulation points for different times are observed to collapse onto each other very well. In simulations, two sets of $g_{\rm in}(x)$ over a uniform background having density $\rho_0 = 1.8$ are considered: Step initial density perturbation [Eq. (13)] in panel (a) and wedge-like initial density perturbation [Eq. (14)] in panel (b). Insets: Initial scaled density $g_{\rm in}(x)$ vs scaled position $x = X/L$ is plotted. Lines represent theory, where numerical integration of Eq. (9) is performed, and points represent simulations.

near-critical scaling regime, we use a finite-size scaling of the activity $A(\Delta, L) = L^{-\beta/\nu_\perp}\mathcal{A}(L^{1/\nu_\perp}\Delta)$, with $\mathcal{A}$ being a function of the scaling variable $L^{1/\nu_\perp}\Delta$ [48,55]. Consequently, we obtain a time-evolution equation of the scaled excess density $G(x,\tau) = L^{1/\nu_\perp}\Delta(X,t)$, satisfying a nonlinear diffusion equation $\partial_\tau G(x,\tau) = \partial_x^2 \mathcal{A}(G)$, where space and time are scaled as $x = X/L$ and $\tau = t/L^z$, respectively; here z is the dynamical exponent being determined via the two static exponents β and $\nu_\perp$, where we use the following scaling relation:

$$z = 2 - \frac{(1-\beta)}{\nu_\perp}. \tag{15}$$

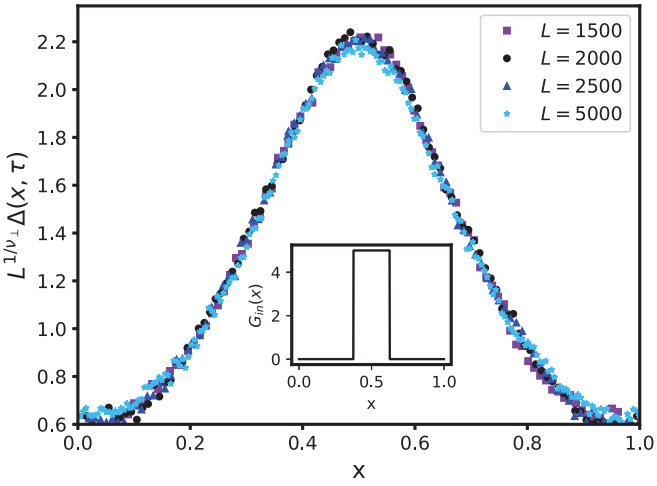

FIG. 3. Verification of superdiffusive scaling near criticality. Plot of the scaled local excess density, denoted as $G(x,\tau) \equiv L^{1/\nu_\perp}\Delta(X = xL, t = \tau L^z)$, against the scaled position x for various times and system sizes: $t_1 = 10\,337$ for $L_1 = 1500$ (depicted by pink squares), $t_2 = 15\,591$ for $L_2 = 2000$ (depicted by black circles), $t_3 = 21\,445$ for $L_3 = 2500$ (depicted by blue triangles), and $t_4 = 57\,725$ for $L = 5000$ (depicted by sky-blue asterisks). The hydrodynamic time is maintained constant at $\tau = t/L^z \simeq 0.3$, with critical exponents set as $z = 10/7$, $\beta = 5/21$, and $\nu_\perp = 4/3$. Remarkably, the simulation points at different times and for various system sizes exhibit a very good scaling collapse. In the inset we plot initial scaled excess density $G_{\rm in}(x)$, defined as $G_{\rm in} = L^{1/\nu_\perp}\Delta(X = xL, t = 0)$, vs scaled position $x = X/L$.

The arguments given above can be verified in simulations. To this end, we study rescaled excess density field $\mathcal{G}(x,\tau)$ starting from a step initial density profile $\mathcal{G}_{\rm in}(x) \equiv \mathcal{G}(x, \tau = 0)$, which is given by

$$G_{\rm in}(x) = \begin{cases} \rho_1 & \text{for } x_1 \leqslant x \leqslant x_2, \\ 0 & \text{otherwise.} \end{cases} \tag{16}$$

We consider here the width of the initial profile $w = 1/4$ and height $\rho_1 \simeq 5.0$ from $x_1 = 1/2 - w/2$ to $x_2 = 1/2 + w/2$. We generate the initial density profile over a uniform critical background density ρ_c. Now we verify the aforementioned "superdiffusive" scaling of the time-dependent density profiles. From this verification, we proceed to test the scaling relation as in Eq. (15) as follows: We consider four systems with sizes $L_1 = 1500$, $L_2 = 2000$, $L_3 = 2500$, and $L_4 = 5000$. These systems evolve from an initial step profile given by Eq. (16) up to times $t_1 = \tau L_1^z$, $t_2 = \tau L_2^z$, $t_3 = \tau L_3^z$, and $t_4 = \tau L_4^z$, with τ held fixed. In this context, we determine the dynamic exponent z by employing the scaling relation (15), by incorporating the previously conjectured static exponents $\beta \simeq 5/21$ and $\nu_\perp \simeq 4/3$ for the conserved Oslo model [27]. As part of our finite-size-scaling argument regarding the bulk-diffusion coefficient, we expect the density profiles, evolved up to the above mentioned times, to exhibit a collapse onto each other. In Fig. 3 we depict the scaled excess density $G(x,\tau)$, defined as $G \equiv L^{1/\nu_\perp}\Delta(X,t)$ and plot against the scaled position $x = X/L$ for four system sizes and times: $t_1 = 10\,337$ for $L_1 = 1500$ (represented by pink squares), $t_2 = 15\,591$ for $L_2 = 2000$ (represented by black circles),

$t_3 = 21\,445$ for $L_3 = 2500$ (represented by blue triangles), and $t_4 = 57\,725$ for $L = 5000$ (represented by sky-blue asterisks). Here we set $\tau = t/L^z \simeq 0.3$, and our analysis involves averaging over 2×10^5 random initial configurations and trajectories. The results demonstrate a quite good collapse of the scaled shifted (excess) density profiles at the final above mentioned times.

3. Density relaxation on critical background

In this section we study density relaxation on an infinite critical background having density ρ_c. The excess density Δ over the critical background is not taken too far away from criticality but much larger than $O(L^{-1/\nu_\perp})$, i.e., we have excess density of order $O(L^{-1/\nu_\perp}) \ll \Delta \lesssim 1$. So the correlation length is still large $\xi \gg 1$ but $k\xi \ll 1$. In this regime, we exactly calculate, within our theory, the asymptotic scaling function for density profiles, which have evolved up to a long time. Near criticality, the activity $a(\Delta)$ as a function of excess density Δ is a power law, i.e., we can write $a(\Delta) \simeq C\Delta^\beta$, where C is the constant of proportionality and β is the order parameter exponent. Now we use the power-law scaling of activity in Eq. (6), and, in that case, the time-evolution equation for excess density can be written as follows:

$$\frac{\partial \Delta(X,t)}{\partial t} = C\frac{\partial^2[\Delta(X,t)]^\beta}{\partial X^2}. \tag{17}$$

To study the density relaxation in this regime, we take initial condition having a form of delta function $\Delta(X, t=0) = N_1\delta(X)$, with N_1 number of particles added at the midpoint, to create the initial perturbation over the critical background. The reason for taking such an initial condition is that here we are interested to study evolution of a localized initial density profile on an infinite critical background on a large space and time scales. In that case, it is interesting that, for the following boundary condition $\Delta(x = \pm\infty, t) = 0$, the nonlinear diffusion equation (17) can exactly be solved. We consider a scaling ansatz of the excess density as

$$\Delta(X,t) = \frac{1}{(Ct)^\omega}\mathcal{G}\left[\frac{X}{(Ct)^\omega}\right], \tag{18}$$

where the scaling function is $\mathcal{G}(y)$ satisfies the differential equation

$$\frac{d^2\mathcal{G}^\beta}{dy^2} = \omega\left[\mathcal{G} + y\frac{d\mathcal{G}}{dy}\right], \tag{19}$$

where the growth exponent is given by $\omega = 1/(1+\beta)$; for the Oslo model, $\beta < 1$ and therefore $\omega > 1/2$. By solving Eq. (19), we exactly have

$$\mathcal{G}(y) = \frac{1}{\left[g_0^{\beta-1} + \frac{\omega(1-\beta)}{2\beta}y^2\right]^{1/(1-\beta)}}, \tag{20}$$

with the suitable choice of boundary conditions, $\mathcal{G}(y=0) = g_0$ and $[d\mathcal{G}/dy]_{y=0} = 0$, where g_0 is the normalization constant, being proportional to the number of particles added initially in the system.

Next, we verify the above scaling solution in simulations. At initial time $t = 0$, we consider a localized density profile,

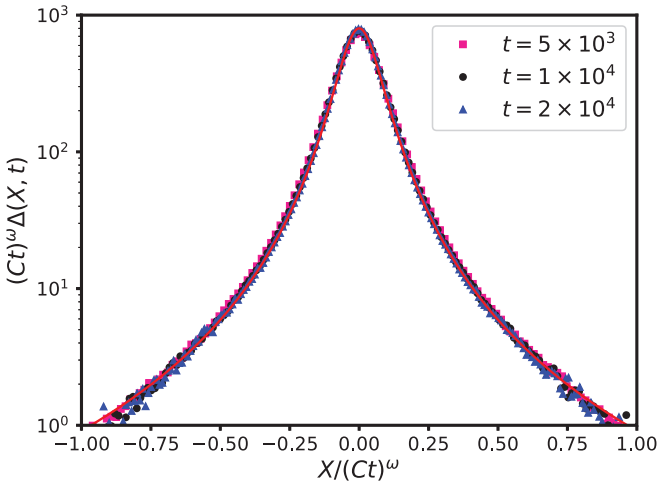

FIG. 4. Density relaxation on critical background. We plot scaled excess density profile $(Ct)^\omega\Delta(X,t)$, where $\Delta(X,t) = [\rho(X,t) - \rho_c]$, against scaling variable $X/(Ct)^\omega$ for times $t = 2 \times 10^4$ (blue triangles), 10^4 (black circles), and 5×10^3 (pink squares). The initial density profile is chosen to be a Gaussian one as in Eq. (21); we take $N_1 = 150$. Red line and points represent theory [Eq. (20)] and simulations, respectively.

which has a Gaussian form,

$$\Delta(X, t=0) = N_1\frac{1}{\sqrt{2\pi w^2}}e^{-X^2/2w^2}, \tag{21}$$

where the width of the initial profile is taken $w = 10$ and in simulation $N_1 = 150$ number of particles are distributed according to the Gaussian distribution function [Eq. (21)] over an infinite critical background with density ρ_c. In simulation, a system size $L = 5000$ is taken large in comparison to the width δ of the initial density profile, and we also let the initial profile to relax for large times $t \gg 1$ such that, in the large spatial and temporal scales, the initial localized profile reduces to a Dirac-delta function. We compare simulations and the analytical solution as given in Fig. 4 by plotting the scaled excess density $\mathcal{G}(y)$ as a function of y for times $t = 5 \times 10^3$ (pink squares), 10^4 (black circles), and 2×10^4 (blue triangles); the analytical form of the scaling function $\mathcal{G}(y)$ as in Eq. (20) is presented as a red line. We see from the plot that theory and simulation results are in excellent agreement. This particular anomalous spreading in the Oslo model as encoded in Eq. (20), with growth exponent $\omega > 1/2$, should be contrasted with the subdifusive scaling found in a CoM-conserving system with broken time-reversal symmetry [20].

IV. THEORY OF DYNAMIC FLUCTUATION

A. Current fluctuation

1. Definitions and notations

Due to the conserved dynamics of the Oslo model, the microscopic time-evolution equation of local density, as provided in Eq. (4), can be expressed in a form of a microscopic continuity equation. This equation involves the local difference of the microscopic instantaneous particle current operator, denoted as $\mathcal{J}_i(t)$, across the bond $(i, i+1)$ in the

temporal interval $(t, t+dt)$ and can be written as

$$\frac{d\rho_i(t)}{dt} = \langle \mathcal{J}_{i-1}(t) - \mathcal{J}_i(t) \rangle, \tag{22}$$

where we write the average of instantaneous current as $\langle \mathcal{J}_i(t) \rangle = \langle \hat{a}_i(t) - \hat{a}_{i+1}(t) \rangle$. We decompose the instantaneous current as a sum of diffusive current $\mathcal{J}_i^{(d)}(t)$ and fluctuating, or "noise," current $\mathcal{J}_i^{(fl)}(t)$,

$$\mathcal{J}_i(t) = \mathcal{J}_i^{(d)}(t) + \mathcal{J}_i^{(fl)}(t), \tag{23}$$

where we identify the stochastic variable $\mathcal{J}_i^{(d)}(t)$ as

$$\mathcal{J}_i^{(d)}(t) = \hat{a}_i(t) - \hat{a}_{i+1}(t), \tag{24}$$

with $\langle \mathcal{J}_i^{(fl)}(t) \rangle = 0$. Our main goal is to calculate the dynamic correlation function $\langle \mathcal{J}_i(t)\mathcal{J}_j(t') \rangle$ and the fluctuation properties of noise current $\mathcal{J}_i^{(fl)}(t)$. To this end, we define the time-integrated bond current $\mathcal{Q}_i(t)$, which represents cumulative (time-integrated) particle current across bond $(i, i+1)$ in a time interval $[0, t]$ and is related to instantaneous current $\mathcal{J}_i(t)$ as

$$\mathcal{J}_i(t) = \frac{d}{dt'} \mathcal{Q}_i(t') \Big|_{t'=t}. \tag{25}$$

From the dynamic correlations of time-integrated current $\langle \mathcal{Q}_i(t)\mathcal{Q}_j(t') \rangle$, we can find the dynamic correlation of instantaneous current as

$$\langle \mathcal{J}_i(t)\mathcal{J}_j(t') \rangle = \frac{d}{dt}\frac{d}{dt'} \langle \mathcal{Q}_i(t)\mathcal{Q}_j(t') \rangle, \tag{26}$$

for any arbitrary values of t and t'. We introduce the following notation for correlation function:

$$C_r^{AB}(t, t') = \langle A_r(t) B_{i+r}(t') \rangle - \langle A_r(t) \rangle \langle B_{i+r}(t') \rangle, \tag{27}$$

whereas the stationary correlation functions are defined as $C_r^{AB}(t) = C_r^{AB}(t, 0)$. Also, here we define the Fourier transform of the correlation functions $C_r^{AB}(t, t')$ in the spatial domain of r as

$$\tilde{C}_q^{AB}(t, t') = \sum_{r=0}^{L-1} C_r^{AB}(t, t') e^{\mathbf{i}qr}, \tag{28}$$

where we have $q = 2\pi k/L$ with $k = 0, 1, \ldots, L-1$; then the inverse Fourier transform can be written as

$$C_r^{AB}(t, t') = \frac{1}{L} \sum_q \tilde{C}_q^{AB}(t, t') e^{-\mathbf{i}qr}, \tag{29}$$

with $\mathbf{i}^2 = -1$.

2. *Correlation of integrated current and the truncation scheme*

In this section we study the unequal-space-time correlation of the integrated bond current $\mathcal{Q}$ starting from writing the evolution equations, which can be obtained from the following infinitesimal-time update rules for the quantity $\langle \mathcal{Q}_i(t+dt)\mathcal{Q}_{i+r}(t') \rangle$:

$$\mathcal{Q}_i(t+dt)\mathcal{Q}_{i+r}(t') = \begin{cases} \text{events} & \text{probabilities} \\ (\mathcal{Q}_i(t)+1)\mathcal{Q}_{i+r}(t') & \hat{a}_i(t)dt \\ (\mathcal{Q}_i(t)-1)\mathcal{Q}_{i+r}(t') & \hat{a}_{i+1}(t)dt \\ \mathcal{Q}_i(t)\mathcal{Q}_{i+r}(t') & 1-\Sigma dt, \end{cases} \tag{30}$$

for $t > t'$, where $\Sigma = (\hat{a}_i(t) + \hat{a}_{i+1}(t))$. From the above update rules, we obtain the time-evolution equation for the two-point correlation function involving integrated bond current,

$$\frac{d}{dt} C_r^{\mathcal{Q}\mathcal{Q}}(t, t') = \langle \{\hat{a}_i(t) - \hat{a}_{i+1}(t)\} \mathcal{Q}_{i+r}(t') \rangle, \tag{31}$$

solving which, we obtain the exact expression for the unequal-time unequal-space correlation function of the integrated current, $C_r^{\mathcal{Q}\mathcal{Q}}(t, t')$, as

$$C_r^{\mathcal{Q}\mathcal{Q}}(t, t') = \int_{t'}^{t} dt'' \left\langle \mathcal{J}_i^{(d)}(t'') \mathcal{Q}_{i+r}(t') \right\rangle + C_r^{\mathcal{Q}\mathcal{Q}}(t', t'), \tag{32}$$

where $\mathcal{J}_i^{(d)}(t'')$ on the right-hand side of the above equation is given by Eq. (24). Note that, in Eqs. (31) and (32) (also later throughout), we omit all terms containing the average of the integrated current, $\langle \mathcal{Q}_i(t) \rangle$, since we are concerned only with the steady state where $\langle \mathcal{Q}_i(t) \rangle = 0$ due to the periodic boundary condition and the absence of any biasing force.

To further simplify the Eq. (32), we need to calculate the unequal-time unequal-space correlation function for the diffusive current and the time-integrated current, which involves the dynamic correlation function of activity and integrated current. It is not difficult to see that the corresponding evolution equation, $d\langle \hat{a}_i(t)\mathcal{Q}_{i+r}(t') \rangle/dt$, generates more higher-order correlation functions and an infinite hierarchy among them. Now we employ an approximate closure scheme along the lines of what was introduced in the context of the conserved Manna model [48]. The closure scheme is incorporated by expressing the microscopic diffusive current across a bond in terms of the difference in local mass between two neighboring sites connected by that specific bond as

$$\mathcal{J}_i^{(d)}(t) \simeq D(\bar{\rho})(m_i(t) - m_{i+1}(t)), \tag{33}$$

where $D(\bar{\rho}) = a'(\bar{\rho})$ is the bulk-diffusion coefficient as defined in Eq. (7). In Eq. (33) we assume that any difference in local activity should follow the difference in local mass. This implies that the diffusive current is proportional to the local mass difference, with an additional assumption that fluctuations are quite small, allowing us to express the bulk diffusion coefficient obtained for the corresponding global density as the proportionality constant. The approximation in Eq. (33) essentially implies that, involving any correlation function involving diffusive current and another dynamic quantity, we should substitute the diffusive current with Eq. (33); for example, consider the following correlation function:

$$\begin{aligned} \left\langle \mathcal{J}_i^{(d)}(t) A_{i+r}(t') \right\rangle &= \langle \{\hat{a}_i(t) - \hat{a}_{i+1}(t)\} A_{i+r}(t') \rangle \\ &\simeq D(\bar{\rho}) \langle \{m_i(t) - m_{i+1}(t)\} A_{i+r}(t') \rangle, \end{aligned} \tag{34}$$

where A could be any dynamic observable. Now, by substituting Eq. (33) in Eq. (32) we obtain

$$C_r^{\mathcal{Q}\mathcal{Q}}(t,t') \simeq a'(\bar{\rho}) \int_{t'}^{t} dt'' \langle \{m_i(t'') - m_{i+1}(t'')\} \mathcal{Q}_{i+r}(t') \rangle + C_r^{\mathcal{Q}\mathcal{Q}}(t',t'), \tag{35}$$

which requires the correlation function $C_r^{m\mathcal{Q}}(t,t')$ instead of the correlation involving activity variable and integrated current. For convenience, we switch to the Fourier representation of $C_r^{m\mathcal{Q}}(t,t')$,

$$\tilde{C}_q^{m\mathcal{Q}}(t,t') = \exp[-a'(\bar{\rho})\lambda_q(t-t')]\tilde{C}_q^{m\mathcal{Q}}(t',t'), \tag{36}$$

where $\lambda_q = 2(1-\cos q)$ are the eigenvalues of the discrete Laplacian; for details see Appendix A. Although Eq. (35) along with Eq. (36) completely describes the dynamical correlations of the time-integrated bond current, we need to calculate the equal-time correlation of current and mass to obtain the complete solution. The Fourier mode of the equal-time correlation function is given by

$$\tilde{C}_q^{m\mathcal{Q}}(t,t) = \int_0^t dt' \exp[-a'(\bar{\rho})\lambda_q(t-t')]\tilde{f}_q(t'), \tag{37}$$

where the Fourier mode of a source term is

$$\tilde{f}_q = ae^{-\mathbf{i}2q}(e^{\mathbf{i}q}-1)^3 + \tilde{C}_q^{m\hat{a}}(1-e^{-\mathbf{i}q}); \tag{38}$$

for details see Appendix B.

We next calculate the correlation function $C_r^{m\hat{a}}$ by using the steady-state condition of equal time two-point spatial mass correlation function, $dC_r^{mm}(t,t)/dt = 0$, from which we obtain

$$C_r^{m\hat{a}}(\bar{\rho}) = a(\bar{\rho})\delta_{0,r} - \frac{a(\bar{\rho})}{2}(\delta_{0,r-1} - \delta_{0,r+1}); \tag{39}$$

for details see Appendix C. The Fourier transform of $C_r^{m\hat{a}}$ is $\tilde{C}_q^{m\hat{a}}(\bar{\rho}) = a(\bar{\rho})\lambda_q/2$ and used in Eq. (38) to obtain

$$\tilde{f}_q(\bar{\rho}) = -a(\bar{\rho})\frac{\lambda_q}{2}(1-e^{-iq}). \tag{40}$$

By substituting Eq. (40) in Eq. (37) and then putting Eq. (37) into Eq. (36), we finally obtain the Fourier transform of unequal-time mass and integrated current as

$$\tilde{C}_q^{m\mathcal{Q}}(t,t') = -a(\bar{\rho}) \int_0^{t'} dt'' e^{-a'(\bar{\rho})\lambda_q(t-t'')} \frac{\lambda_q}{2}(1-e^{-iq}). \tag{41}$$

Now, to obtain an explicit expression of the dynamic current correlation function in Eq. (35), we need to calculate the equal-time correlation of the integrated current, which is given on the right-hand side of Eq. (35). On the other hand, the first integral on the right-hand side is explicitly computed by using the inverse Fourier transform of Eq. (41). It can be shown, from the infinitesimal-time evolution of the product $\mathcal{Q}_i(t+dt)\mathcal{Q}_{i+r}(t+dt)$, that the equal-time integrated current correlation satisfies the following:

$$\begin{aligned} \frac{d}{dt}C_r^{\mathcal{Q}\mathcal{Q}}(t,t) &= \Gamma_r(t) + C_r^{\mathcal{J}^{(d)}\mathcal{Q}}(t,t) + C_{L-r}^{\mathcal{J}^{(d)}\mathcal{Q}}(t,t), \\ &\simeq \Gamma_r(t) + a'\left\{C_r^{m\mathcal{Q}}(t,t) - C_{r-1}^{m\mathcal{Q}}(t,t)\right\} \\ &\quad + a'\left\{C_{L-r}^{m\mathcal{Q}}(t,t) - C_{L-r-1}^{m\mathcal{Q}}(t,t)\right\}, \end{aligned} \tag{42}$$

where we denote Γ_r as the strength of the fluctuating current with $\langle \mathcal{J}_i^{(fl)}(t)\mathcal{J}_{i+r}^{(fl)}(t')\rangle = \Gamma_r\delta(t-t')$[48]. Using microscopic dynamics (see Appendix D), the quantity $\Gamma_{i,j} \equiv \Gamma_r$, with $r = |j-i|$, can be written as

$$\Gamma_{i,j} = u_{i,j} - u_{i+1,j}, \tag{43}$$

where $u_{i,j}$ is given by

$$u_{i,j} = a_i(\delta_{i,j} - \delta_{i-1,j}). \tag{44}$$

In the steady state, we can simply write

$$\Gamma_r(\bar{\rho}) = 2a(\bar{\rho})\delta_{0,r} - a(\bar{\rho})\delta_{0,r+1} - a(\bar{\rho})\delta_{0,r-1}; \tag{45}$$

for details see Appendix D. We thus obtain the full solution of Eq. (42), i.e., the second part of Eq. (35), by substituting the inverse Fourier transform of Eq. (37) for equal-time mass and integrated current correlation. Finally, using the inverse Fourier transform of Eq. (41) in Eq. (35) and the solution of Eq. (42), we get the unequal-time unequal-space correlation function of the integrated current for $t \geqslant t'$ as

$$\begin{aligned} C_r^{\mathcal{Q}\mathcal{Q}}(t,t') = &\int_0^{t'} dt''\Gamma_r(t'') - \frac{a'(\bar{\rho})a(\bar{\rho})}{L}\sum_q \int_0^{t'} dt'' \int_0^{t''} dt''' e^{-a'(\bar{\rho})\lambda_q(t''-t''')}\frac{\lambda_q^2}{2}[2-\lambda_{qr}] \\ &- \frac{a'(\bar{\rho})a(\bar{\rho})}{L}\sum_q \int_t^{t'} dt'' \int_0^{t'} dt''' e^{-a'(\bar{\rho})\lambda_q(t''-t''')}\frac{\lambda_q^2}{2}e^{-\mathbf{i}qr}. \end{aligned} \tag{46}$$

Notably, the above expression is subtly different from that in the Manna sandpile studied in Ref. [48]. Indeed, it has significant ramifications for the exponents for temporal decay of current correlations and for the mobility. To understand the consequences of Eq. (46), and fluctuating hydrodynamics of the Oslo model, in the next section we study the space-time-integrated current.

3. *Fluctuating current and its relation to total current*

We first investigate the dynamic correlation function for the fluctuating part $\mathcal{J}_i^{(fl)}(t)$ of the instantaneous bond current, as defined in Eq. (23), and we have

$$C_r^{\mathcal{J}^{(fl)}\mathcal{J}^{(fl)}}(t,t'=0) \equiv C_r^{\mathcal{J}^{(fl)}\mathcal{J}^{(fl)}}(t) = \delta(t)\Gamma_r(\bar{\rho}), \tag{47}$$

where Γ_r is given in Eq. (45). We define the time-integrated fluctuating current $\mathcal{Q}_i^{(fl)}(T) = \int_0^T dt\, \mathcal{J}_i^{(fl)}$ across a bond up to time T. The scaled variance of the time-integrated fluctuating bond current is obtained from

$$\lim_{T\to\infty} \frac{1}{T}\langle [\mathcal{Q}_i^{(fl)}(T)]^2\rangle_c = \int_{-\infty}^{\infty} C_0^{\mathcal{J}^{(fl)}\mathcal{J}^{(fl)}}(t)\, dt, \tag{48}$$

and, by setting $r = 0$ in Eq. (45), we immediately obtain a fluctuation relation,

$$\lim_{T\to\infty} \frac{1}{T}\langle [\mathcal{Q}_i^{(fl)}(T)]^2\rangle_c = \Gamma_0 = 2a(\bar{\rho}). \tag{49}$$

Remarkably, the scaled variance of the space-time-integrated fluctuating current is identically *zero*, i.e., we have

$$\lim_{T,L\to\infty} \frac{1}{LT}\left\langle \left[\sum_i \mathcal{Q}_i^{(fl)}(T)\right]^2\right\rangle_c = \sum_r \int_{-\infty}^{\infty} C_r^{\mathcal{J}^{(fl)}\mathcal{J}^{(fl)}}(t)\, dt = \sum_r \Gamma_r = 0. \tag{50}$$

We also define the space-time-integrated actual particle current $\bar{Q}(L,T) = \sum_{i=0}^{L-1} \mathcal{Q}_i(T)$ in a system of size L and up to time T, and study the variance $\langle \bar{Q}^2(L,T)\rangle_c = \langle \bar{Q}^2(L,T)\rangle - \langle \bar{Q}(L,T)\rangle^2$ in the steady state. As previously discussed for a diffusive system in Ref. [48], the variance of the space-time-integrated current is directly related to the density-dependent particle mobility $\chi(\rho) = \lim_{L\to\infty} \langle \bar{Q}^2(L,T)\rangle/2LT$. Indeed, it is not difficult to see that the variance of the space-time-integrated actual current is related to the variance of fluctuating current as

$$\lim_{L\to\infty} \frac{\langle \bar{Q}^2(L,T)\rangle_c}{LT} = \sum_r \Gamma_r, \tag{51}$$

which, by using Eq. (50), immediately leads the particle mobility to exactly vanish, i.e., $\chi = 0$ in the Oslo model. As seen later, this result is consistent with our finding that the bond-current fluctuation $\langle \mathcal{Q}_i^2(T)\rangle$ in the Oslo model in fact saturates in the long-time limit [see Eq. (53)]. That is, for $T \gg L^2$, the time derivative $d\langle \mathcal{Q}_i^2(T)\rangle/dT$, being equal to $2\chi/L$ [see Eq. (54)], is identically zero. We now verify Eq. (49) in simulations. In Fig. 5 we plot (solid blue line, simulations) $\langle [\mathcal{Q}_i^{(fl)}(T)]^2\rangle/T$ as a function of the relative density $\Delta = \bar{\rho} - \rho_c$. We observe an excellent agreement with twice the activity (black dotted line) as predicted by theory Eq. (49).

4. Bond current fluctuation: Away from criticality

Now the second cumulant, or the variance, $\langle \mathcal{Q}_i^2(T)\rangle_c = \langle \mathcal{Q}_i^2(T)\rangle$, of the time-integrated bond current in the steady state can immediately be obtained from Eq. (46), by setting $r = 0$ and $t = t' = T$,

$$\langle \mathcal{Q}_i^2(T,L,\bar{\rho})\rangle = \frac{a(\bar{\rho})}{a'(\bar{\rho})}\frac{1}{L}\sum_q (1 - e^{-a'(\bar{\rho})\lambda_q T}) \simeq \frac{aT^{-1/2}}{2\sqrt{\pi}(a')^{\frac{3}{2}}}, \tag{52}$$

where the asymptotic form is valid for large T; for details, see Appendix F 1. Note that, unlike the conserved Manna sandpile [48] or the symmetric simple exclusion processes [59], where there is a single conserved quantity, the bond-current fluctuation $\langle \mathcal{Q}_i^2(T,L,\bar{\rho})\rangle$ in the Oslo model, for any fixed $\bar{\rho}$ and in the limit of large time $T \gg L^2 \gg 1$, saturates to a finite value $\Sigma_Q^2(\bar{\rho})$. That is, we have the existence of the following limit:

$$\lim_{L\to\infty}\Big[\lim_{T\to\infty}\big\langle \mathcal{Q}_i^2(T,L,\bar{\rho})\big\rangle\Big] \equiv \Sigma_Q^2(\bar{\rho}) = \frac{a}{a'}. \tag{53}$$

Note that we take the infinite-time limit first and then the infinite-system-size limit. For diffusive systems, the transport coefficient, which characterizes current fluctuation in the system, is the mobility $\chi(\bar{\rho})$ (or equivalently, mobility) and is defined as

$$\lim_{T\to\infty} \frac{\big\langle \mathcal{Q}_i^2(T,L,\bar{\rho})\big\rangle}{T} \equiv 2\frac{\chi(\bar{\rho})}{L}. \tag{54}$$

Remarkably, in the long-time limit ($T \gg L^2$), the vanishing temporal growth of the variance of the time-integrated bond current in the Oslo model leads to the vanishing particle mobility $\chi(\bar{\rho}) = 0$, a direct consequence of the deterministic particle transfer during a toppling event.

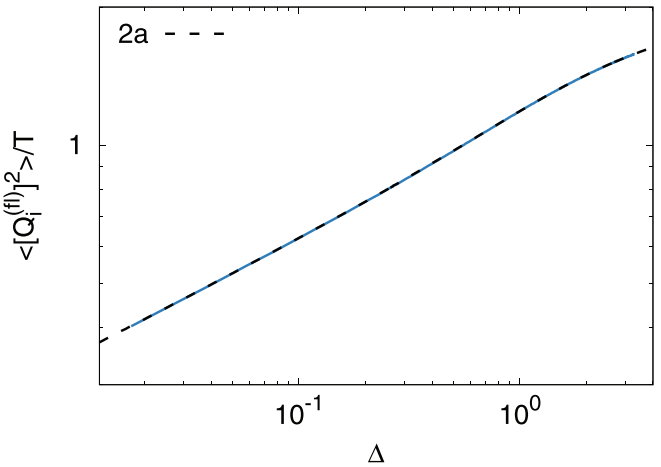

FIG. 5. Scaled variance $\langle [\mathcal{Q}_i^{(fl)}(T)]^2\rangle_c/T = \langle [\mathcal{Q}_i^{(fl)}(T)]^2\rangle/T$ of time-integrated fluctuating (or noise) current is plotted as a function of relative density $\Delta = \bar{\rho} - \rho_c$ ($\rho_c \approx 1.732$) for system sizes $L = 1000$ and $T = 100$ (solid blue line). We also plot $2a(\Delta)$ as a function of Δ (dotted black line). Simulations are in excellent agreement with theory [Eq. (50)].

B. Mass fluctuation

The dynamic fluctuation properties of the mass in a subsystem is another important quantity that we study in this section. To calculate the fluctuation of the mass of a subsystem of size l, $M_l(t) = \sum_{i=0}^{l=1} m_i(t)$, we begin with the steady-state correlation function of the unequal time and the unequal space of the mass of a single site for $t \geqslant 0$, $C_r^{mm}(t,0) = \langle m_i(t) m_{i+r}(0)\rangle - \langle m_i(t)\rangle\langle m_{i+r}(0)\rangle \equiv C_r^{mm}(t)$. Due to the microscopic dynamics that permit simultaneous mass changes in three sites, we anticipate the presence of spatial correlations in current in the steady state. We have the Fourier modes of $C_r^{mm}(t)$,

$$\tilde{C}_q^{mm}(t) \simeq e^{-a'(\bar{\rho})\lambda_q t}\tilde{C}_q^{mm}(0), \tag{55}$$

where the factor $\tilde{C}_q^{mm}(0)$ represents the Fourier transform of the (equal-time) two-point spatial correlation function for

mass; see Appendix E for details. In the steady state, the correlation function $C_r^{mm}(0)$ can be obtained by using the condition $dC_r^{mm}(t,t)/dt = 0$, i.e.,

$$2a'\langle(m_{i+1} - 2m_i + m_{i-1})m_{i+r}\rangle_c + B_r \simeq 0, \tag{56}$$

where the source term

$$B_r = a[6\delta_{0,r} - 4(\delta_{0,r+1} + \delta_{0,r-1}) + (\delta_{0,r+2} + \delta_{0,r-2})], \tag{57}$$

and we use the approximation (33); for details, see Eqs. (C4) and (C5) in Appendix C. Finally, solving the above equation, we simply have

$$C_r^{mm}(0) \simeq \frac{a}{a'}\delta_{0,r} - \frac{a}{2a'}(\delta_{0,r-1} + \delta_{0,r+1}). \tag{58}$$

By substituting the Fourier mode $\tilde{C}_q^{mm}(0) = (a/2a')\lambda_q$ in Eq. (55), we have

$$\tilde{C}_q^{mm}(t) \simeq e^{-a'\lambda_q t}\frac{a}{2a'}\lambda_q. \tag{59}$$

Finally, using the inverse Fourier transform of $\tilde{C}_q^{mm}(t)$, we get the desired correlation function,

$$C_r^{mm}(t) \simeq \frac{1}{L}\frac{a}{2a'}\sum_q e^{-iqr}e^{-a'\lambda_q t}\lambda_q. \tag{60}$$

We use the above equation to compute the dynamic correlations for mass $M_l(t) = \sum_{r=0}^{l-1} m_r(t)$ in a subsystem of size l through the following identity:

$$C^{M_lM_l}(t) = lC_0^{mm}(t) + \sum_{r=1}^{l-1}(l-r)\big[C_r^{mm}(t) + C_{-r}^{mm}(t)\big]. \tag{61}$$

By substituting Eq. (60) into the above equation, we get

$$C^{M_lM_l}(t) \simeq \frac{1}{L}\frac{a}{2a'}\sum_q e^{-a'\lambda_q t}\lambda_{ql}. \tag{62}$$

For $l \gg 1$, $L \gg 1$, and $l/L \ll 1$, by using $\lambda_{ql} \simeq 2$ replacing the sum as an integral, and then substituting $z = 4\pi^2 a' x^2 t$, we obtain

$$C^{M_lM_l}(t) \simeq \frac{2a}{a'}\int_{1/L}^{1/2} e^{-a'\lambda(x)t}dx \simeq \frac{a}{2\sqrt{\pi}a'^{3/2}}t^{-1/2}, \tag{63}$$

which decays with time as $t^{-1/2}$. Note that this particular asymptotic decay is qualitatively different from that for the Manna sandpile, where, far from criticality, $C^{M_lM_l}(0) - C^{M_lM_l}(t)$ grows as $t^{1/2}$ [48]. Equivalently, the small-frequency power spectrum, for the Manna sandpile and the Oslo model, diverges as $f^{-3/2}$ [48] and $f^{-1/2}$, respectively [see Eq. (83)]. Physically the far-from-critical decay of current correlations (or subsystem-mass fluctuations) in the Oslo model, due to the additional CoM conservation law, is much faster (smaller) compared to that in the Manna sandpile with a single conservation law. The equal-time correlation of subsystem mass can be written by putting $t = 0$ in Eq. (62),

$$C^{M_lM_l}(0) = \langle M_l^2\rangle - \langle M_l\rangle^2 \equiv \Sigma_M^2(\bar{\rho}, l), \tag{64}$$

which, in the limit of subsystem size $l \to \infty$, converges to a finite value and can be written as a function of global density

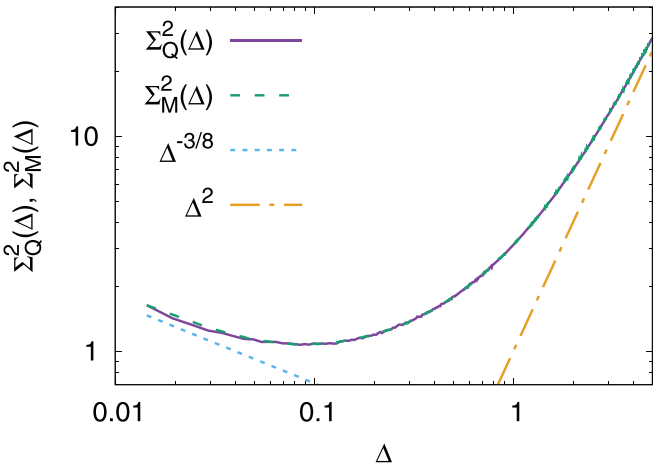

FIG. 6. Comparison of the variance $\Sigma_Q^2(\Delta)$ and $\Sigma_M^2(\Delta)$ of bond current and subsystem mass, respectively, is plotted as a function of relative density $\Delta = \bar{\rho} - \rho_c$. Simulations for current fluctuations are represented as a solid violet line ($L = 1000$); simulations for mass fluctuation are shown as a dashed green line ($L = 1000$ and $l = 500$). Data show an excellent agreement with theory [Eq. (66)]. The dotted line on the left and the dot-dashed line on the right indicate near- and far-from-critical divergence $\Delta^{-3/8}$ and Δ^2, respectively.

only:

$$\Sigma_M^2(\bar{\rho}) \equiv \lim_{l\to\infty}\Sigma_M^2(\bar{\rho}, l) = \frac{a}{a'}. \tag{65}$$

Here we have already taken the thermodynamic limit $L \to \infty$ with $l/L \to 0$. In diffusive systems with a single conservation law (such as symmetric exclusion process or the Manna sandpile away from criticality), the subsystem mass fluctuation as in Eq. (64) grows as l, which, however, is not the case here. As we discuss later in the context of static structure factor, this particular observation is related to an extreme form of hyperuniformity (class I). Moreover, by comparing Eq. (53) and Eq. (65), we immediately obtain the following identity:

$$\Sigma_Q^2(\bar{\rho}) = \Sigma_M^2(\bar{\rho}), \tag{66}$$

which relates the asymptotic (dynamic) bond current fluctuation to the asymptotic (static) subsystem-mass fluctuation. We mention here that, while it captures the dynamic properties of the system remarkably well, the closure scheme is not strictly applicable in the near-critical regime since the spatial correlations in that case become long-ranged and are not captured in the calculations. However, the fluctuation relation, as in Eq. (66), is a direct consequence of a mass-conservation principle (discussed below) and holds both near and far from criticality (see Fig. 6). Importantly, as argued later, Eq. (66) can be used to determine the exponent governing the near-critical temporal growth of the current in terms of the standard static exponents. Indeed the relation in Eq. (66) could be physically understood from a mass-conservation principle as follows. Let us consider a spatial domain $[0, l-1]$ of size l and having mass $M_l(t)$ at time t. Now the time-integrated boundary current $\mathcal{Q}^B(t) = \mathcal{Q}_{-1}(t) - \mathcal{Q}_{l-1}(t)$ flowing into the subsystem in a time interval $[0, t]$ is identically equal to the difference in the subsystem mass $\Delta M_l(t) = M_l(t) - M_l(0)$ at two times $t = 0$ and t. Therefore, the

corresponding fluctuations are also equal, i.e., $\langle[\mathcal{Q}^B(t)]^2\rangle = \langle[\Delta M_l(t)]^2\rangle = \langle[M_l(0)]^2\rangle + \langle[M_l(t)]^2\rangle - 2\langle M_l(0)M_l(t)\rangle$; the equality is valid for any time t and can be suitably generalized to higher dimensions. Now, by first taking the infinite-time limit and then the infinite-subsystem (and infinite-system) limit (i.e., $t \gg L^2$ and $L \gg l \gg 1$), and then assuming complete decorrelation between $M_l(t)$ and $M_l(0)$ [as shown in Eq. (63)] as well as that between $\mathcal{Q}_{-1}(t)$ and $\mathcal{Q}_{l-1}(t)$, we recover the relation as given in Eq. (66). It should be noted here that the above scaling limit does not exist in the case of the conserved-mass Manna sandpile, and also other diffusive systems with a single conservation law, for which the time-integrated boundary current fluctuations $\langle\mathcal{Q}_l^2(t)\rangle$ or $\langle[\mathcal{Q}^B(t)]^2\rangle$, and therefore $\langle[\Delta M_l(t)]^2\rangle$, grow with time.

C. Comparison: Theory and simulations

1. The mass-conservation principle and its consequences

To numerically verify Eq. (66), in Fig. 6 we plot the variance $\Sigma_Q^2(\Delta)$ (solid violet line) and $\Sigma_M^2(\Delta)$ (dashed green line) of the bond current and subsystem mass, respectively, obtained from simulations, as a function of $\Delta = \bar{\rho} - \rho_c$. The comparison between the two quantities substantiates the validity of the relation as in Eq. (66). From the same figure, we also find that the density dependence of Σ_M^2 (and Σ_Q^2) has two qualitatively distinct regimes, a far-from-critical regime and a near-critical one. The asymptotic behavior of subsystem-mass fluctuation as a function of density is given by

$$\Sigma_M^2(\Delta) \sim \begin{cases} \Delta^2 & \text{for } \Delta \gg \rho_c \\ \Delta^{-\delta} & \text{for } \Delta \to 0^+, \end{cases} \tag{67}$$

where the exponent δ has not yet been reported in the literature to the best of our knowledge and is determined below in terms of the standard exponents. *Far from criticality*, we observe, from Eq. (65), that the subsystem-mass fluctuation does not depend on the size of subsystem, i.e., the fluctuation is greatly suppressed. By using Eq. (58)), we see that such an extreme suppression of mass fluctuation is because the integrated density correlations vanish and the subsystem mass fluctuation depends only on the correlations among masses at the boundary sites. Therefore, the density fluctuation is maximally hyperuniform, and, far from criticality, we observe in the Oslo model *"class I"* hyperuniformity [32,33]. We shall discuss this point later when we explicitly calculate the structure factor in this regime. Furthermore, far from criticality, the activity behaves as $a(\Delta) \sim 1 - \text{const}/\Delta$, which can be used in Eq. (65) to obtain $\Sigma_M^2(\Delta) \sim \Delta^2$ for $\bar{\rho} \gg \rho_c$. On the other hand, near-critical behavior of $\Sigma_M^2(\Delta)$ is obtained by using Eq. (66) as follows. It is known that, as $\Delta \to 0$, the subsystem mass fluctuation becomes hyperuniform and scales with system size L as [27]

$$\Sigma_M^2 \sim L^\zeta \sim L^{2(1-1/\nu_\perp)}, \tag{68}$$

where $\zeta = 2(1 - 1/\nu_\perp)$ and $\nu_\perp$ are the hyperuniformity and correlation length exponents, respectively. We then obtain the exponent δ by using the finite-size scaling relation $L \sim \Delta^{-\nu_\perp}$ in Eq. (68),

$$\delta = \frac{\zeta}{\nu_\perp} = \frac{2(1-1/\nu_\perp)}{\nu_\perp} = \frac{3}{8}, \tag{69}$$

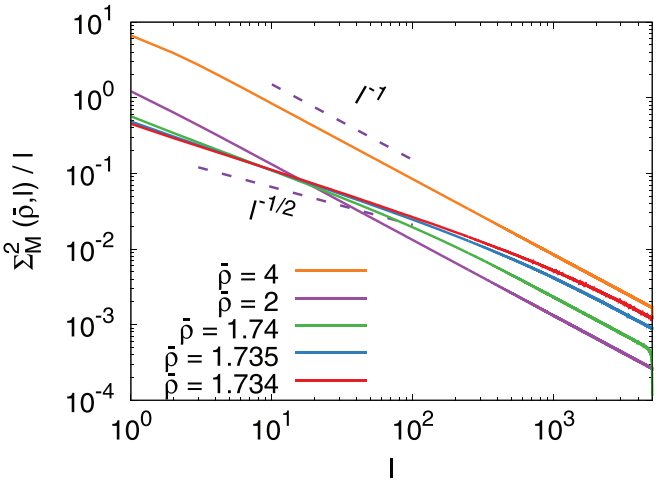

FIG. 7. Scaled variance $\Sigma_M^2(\bar{\rho}, l)/l$ of subsystem mass plotted as a function of subsystem size l. Simulation data for $\bar{\rho} = 4$ (orange line), 2 (violet line), and 1.74 (green line) are obtained for $L = 5000$, whereas data for $\bar{\rho} = 1.735$ (blue line) and 1.734 (red line) are plotted for $L = 10\,000$. Away from criticality, the scaled variance $\Sigma_M^2(\bar{\rho}, l)/l$ of subsystem mass decays as l^{-1}, indicating $\Sigma_M^2(\bar{\rho}, l)$ itself does not depend on subsystem size for $l \gg 1$ (upper guiding line). However, near criticality, $\Sigma_M^2(\bar{\rho}, l)/l \sim l^{-1/2}$, implying $\Sigma_M^2(\bar{\rho}, l) \sim l^{1/2}$ (lower guiding line) and in agreement with Ref. [27].

where $\nu_\perp = 4/3$ [27]. Now, by using the relation as in Eq. (66), we immediately obtain the following near-critical long-time behavior of bond-current fluctuation:

$$\Sigma_Q^2(\Delta) \sim \Delta^{-3/8}. \tag{70}$$

In Fig. 7 we plot the scaled variance Σ_M^2/l of subsystem mass, obtained from simulations, as a function of subsystem size l for far-from-critical densities $\bar{\rho} = 4$ (violet line), 2 (green line), and 1.74 (blue line) and for near-critical densities $\bar{\rho} = 1.735$ (orange line) and 1.734 (red line). Far from the criticality, we have l^{-1} decay of the scaled fluctuation, implying an extreme hyperuniformity, known as the class I hyperuniformity [32], thus verifying our theory as in Eq. (67). In contrast, near criticality, the decay becomes much slower $l^{-\zeta}$, with $\zeta \simeq 0.5$, indicating enhanced, but still hyperuniform, fluctuations. The slight deviations from the value $\zeta = 1/2$, as reported in [27], are due to the finite-size effects. The transition from the (class I) hyperuniformity with $\zeta = 1$ to hyperuniformity with $\zeta = 1/2$ indicates an increase in near-critical fluctuations not only in the current, but also in mass; this particular feature can be understood in the light of Eq. (66), which indicates a nonmonotonic growth of fluctuation and a growing (eventually diverging at criticality) length scale in the system. This observation is indeed consistent with our results on the bond current fluctuation and the associated power spectrum, discussed later in Secs. IV C 4 and IV C 5.

2. Bond current fluctuation: Far from criticality

In Fig. 8 we plot, as solid lines, the relative integrated current fluctuations, $-[\langle\mathcal{Q}_i^2(T)\rangle - \Sigma_Q^2]$ obtained from simulations as a function of T for density values $\bar{\rho} = 2$ (red), 3 (blue), and 4 (green). The corresponding asymptotic

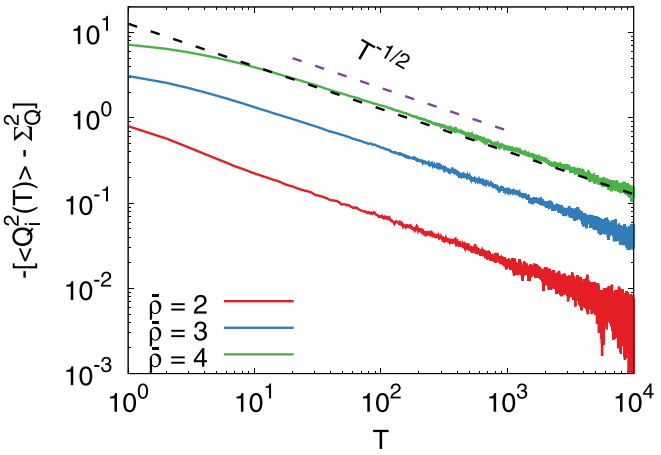

FIG. 8. Relative variance $-[\langle \mathcal{Q}_i^2(T)\rangle - \Sigma_Q^2]$ of the time-integrated bond current is plotted as a function of time for different densities $\bar{\rho} = 2$ (red line), $\bar{\rho} = 3$ (blue line), and $\bar{\rho} = 4$ (green line) and for system size $L = 1000$. We also plot the asymptotic form of the relative variance as a dotted line for $\bar{\rho} = 4.0$, using Eq. (53), which precisely capturers the $T^{-1/2}$ asymptotic decay.

expression of $-[\langle \mathcal{Q}_i^2(T)\rangle - \Sigma_Q^2]$ for $\bar{\rho} = 4.0$ is plotted in the black dotted line using Eq. (53), which is in a nice agreement with simulations at large times. However, near criticality, we observe that the current fluctuation changes drastically, as discussed in the next section.

3. *Bond current fluctuation: Near criticality*

In Fig. 9 we plot the variance $\langle \mathcal{Q}_i^2(T)\rangle_c = \langle \mathcal{Q}_i^2(T)\rangle$ as a function of time for $\bar{\rho} = 1.7344$ (solid red line), $\bar{\rho} = 1.736$ (solid blue line), and $\bar{\rho} = 1.738$ (solid green line). All simulation data are taken for $L = 5000$. A nontrivial crossover

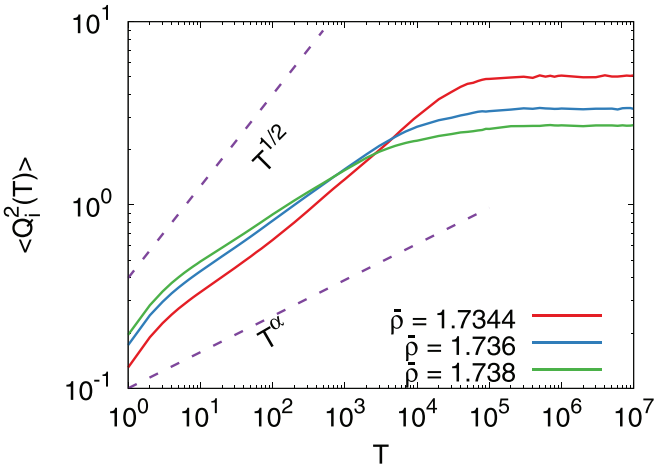

FIG. 9. Variance $\langle \mathcal{Q}_i^2(T)\rangle_c = \langle \mathcal{Q}_i^2(T)\rangle$ of time-integrated bond current near criticality is plotted as a function of time for densities $\bar{\rho} = 1.7344$ (red line), 1.736 (blue line), and 1.738 (green line); system size $L = 5000$. The guiding line representing T^{α} growth is obtained using the theoretically estimated growth exponent $\alpha \simeq 0.197$ from Eq. (73). The other guiding line representing subdiffusive growth $T^{1/2}$ for systems having a single conservation law is plotted for comparison purposes.

as seen in the plot is the following: Although $\langle \mathcal{Q}_i^2(T)\rangle$ for $\bar{\rho} = 1.7344$ has the lowest intensity at the beginning ($T \ll 1$), eventually the corresponding $\Sigma_Q^2(\Delta)$ becomes maximum for $T \gg 1$. This is followed by $\Sigma_Q^2(\Delta)$ for $\bar{\rho} = 1.736$ and then $\Sigma_Q^2(\Delta)$ for $\bar{\rho} = 1.738$. Indeed, we obtain, by using Eq. (66), that $\Sigma_Q^2 \sim \Delta^{-3/8}$ near criticality. Also, the initial time-dependent growth of cumulative current fluctuations is now described by a power law,

$$\left\langle \mathcal{Q}_i^2(T)\right\rangle \sim T^{\alpha}, \tag{71}$$

where the exponent α can be estimated from Eq. (66). As we approach criticality (from above), $\langle \mathcal{Q}_i^2(T)\rangle$ must saturate at $T \simeq L^z$, where z is the dynamic exponent. Now, by using Eq. (71), the corresponding saturation value should have the following near-critical behavior:

$$\lim_{T\to\infty} \left\langle \mathcal{Q}_i^2(T,L)\right\rangle \sim L^{\alpha z} \sim \Delta^{-\delta}, \tag{72}$$

where we use Eq. (67). Then, using the finite-size-scaling $L \simeq \Delta^{-\nu_\perp}$, we have the growth exponent,

$$\alpha = \frac{\delta}{z\nu_\perp}. \tag{73}$$

Substituting the values of $\delta \simeq 3/8$, $z \simeq 10/7$ and $\nu_\perp \simeq 4/3$ [27], we immediately obtain $\alpha \simeq 63/320 \simeq 0.197$, shown as a guiding line T^{α} in Fig. 9 (the other guiding line represents $T^{1/2}$ subdiffusive growth, as observed in diffusive systems with a single conservation law and is provided for comparison purposes). Therefore, the near- and far-from-critical behavior of the time-integrated bond current fluctuation can be written in a combined form,

$$\left\langle \mathcal{Q}_i^2(T)\right\rangle \sim \begin{cases} T^{\alpha} & \alpha = \delta/z\nu_\perp \ \text{ for } \ \bar{\rho} \simeq \rho_c \\ \Sigma_Q^2(\bar{\rho}) - \text{const}\, T^{\alpha} & \alpha = -1/2 \ \text{ for } \ \bar{\rho} \gg \rho_c. \end{cases} \tag{74}$$

As we see later, the exponent α allows us to estimate the exponents for the dynamic correlation functions (and associated power spectra) for the instantaneous bond current as well as subsystem mass fluctuations [see Eqs. (77), (80), and (84)].

4. *Bond current correlation: Far from criticality*

In this section we demonstrate that the (instantaneous) bond-current correlation function decays faster than that in other diffusive systems, such as the Manna sandpile. The bond-current correlation, $C_r^{\mathcal{J}\mathcal{J}}(t) = \langle \mathcal{J}_i(t)\mathcal{J}_{i+r}(0)\rangle - \langle \mathcal{J}_i(t)\rangle\langle \mathcal{J}_{i+r}(0)\rangle$ for $t \geqslant t'$, can be obtained by differentiating Eq. (46) as

$$\begin{aligned} C_r^{\mathcal{J}\mathcal{J}}(t) &= \left[\frac{d}{dt}\frac{d}{dt'} C_r^{\mathcal{Q}\mathcal{Q}}(t,t')\right]_{t'=0,t\geqslant 0} \\ &= \Gamma_r \delta(t) - aa' \frac{1}{L}\sum_q e^{-\lambda_q a' t}\frac{\lambda_q^2}{2} e^{-\mathbf{i}qr}. \end{aligned} \tag{75}$$

The long-time asymptotic form of the above expression with $r = 0$ is given by

$$C_0^{\mathcal{J}\mathcal{J}}(t) \simeq -\frac{3at^{-5/2}}{16\sqrt{\pi}a'^{3/2}}; \tag{76}$$

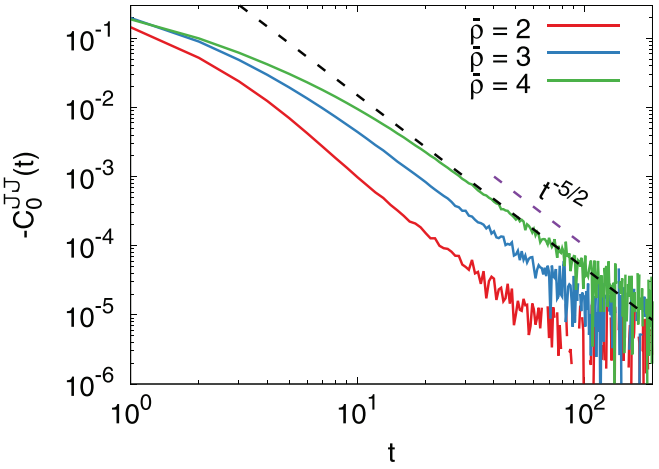

FIG. 10. Far from (above) criticality. Negative of the unequal-time correlation function for bond current $-C_0^{\mathcal{J}\mathcal{J}}(t)$ is plotted as a function of time for different far-from-critical densities. The simulation data are plotted in solid lines for $\bar{\rho} = 2$ (red line), $\bar{\rho} = 3$ (blue line), and $\bar{\rho} = 4$ (green line). The corresponding theoretical asymptotic black dotted line is plotted using Eq. (76) for $\bar{\rho} = 4.0$ and for system size $L = 1000$. The asymptotic line excellently captures the $t^{-5/2}$ power-law decay of the correlation function; it should be contrasted with the conserved Manna sandpiles, for which the decay is $t^{-3/2}$.

for details see Appendix F 2.

In Fig. 10 the negative of the bond-current correlation, $-C_0^{\mathcal{J}\mathcal{J}}(t)$, is plotted as a function of time for different far-from-critical densities. Simulation data are for $\bar{\rho} = 2$ (red line), $\bar{\rho} = 3$ (blue line), and $\bar{\rho} = 4$ (green line) and for system size $L = 1000$. The corresponding theoretical prediction (dotted line), using Eq. (76), is plotted for $\bar{\rho} = 4.0$, indicating $t^{-5/2}$ temporal decay of the correlation function. This is evident that the $t^{-3/2}$ temporal decay for diffusive systems having a single conserved quantity is qualitatively different from the much faster decay (i.e., $t^{-5/2}$) for the Oslo model. From Eq. (74), by taking the derivative of $\langle \mathcal{Q}_i^2(T)\rangle$ twice with respect to time, we can also determine the near-critical asymptotic behavior of unequal-time current correlation function $C_0^{\mathcal{J}\mathcal{J}}(t)$ and express it in terms of $\alpha = \delta/\nu_\perp z$,

$$C_0^{\mathcal{J}\mathcal{J}}(t) \sim -t^{-(2-\alpha)}. \tag{77}$$

That is, we have the following far-from [Eq. (76)] and near-critical behavior of the current correlation function,

$$C_0^{\mathcal{J}\mathcal{J}}(t) \sim \begin{cases} -t^{-(2-\delta/\nu_\perp z)} & \text{for } \bar{\rho} \simeq \rho_c, \\ -t^{-5/2} & \text{for } \bar{\rho} \gg \rho_c. \end{cases} \tag{78}$$

A few remarks are in order. As found previously, for the conserved Manna sandpile in the near-critical regime [48], the decay of the current correlation function is given by $C_0^{\mathcal{J}\mathcal{J}}(t) \sim -t^{-(3/2+\mu)}$ with $\mu > 0$; in fact, the decay is faster compared to the far-from-critical decay of the correlation function (where $\mu = 0$). For the Manna sandpile, this implies a faster suppression of the near-critical dynamical fluctuation of the current as compared to the far-from-critical one. Indeed, in Ref. [48], we called this particular phenomenon, i.e., the "faster-than-usual" decay of the current correlation function, as "dynamical hyperuniformity." For the Oslo model, on the other hand, things are strikingly different. In fact, from Eq. (78), we note that the corresponding values of the *dynamical hyperuniformity* exponents near and far from criticality (from above) are $\mu = (1/2 - \delta/\nu_\perp z) \simeq 0.303$ and $\mu = 1$, respectively. In other words, the dynamical current fluctuation in the Oslo model is actually more enhanced near criticality than it is far from criticality; it is exactly the opposite for the Manna sandpile.

5. Power spectrum: Bond current

Another way to characterize the dynamic fluctuation is to calculate the power spectrum. The power spectrum $S_{\mathcal{J}}(f)$ of the bond current in the steady state can be obtained by taking Fourier transform of the steady-state correlation function $C_0^{\mathcal{J}\mathcal{J}}(t)$ [see Eq. (75) with $r = 0$]. Far from criticality, we obtain an analytical expression for the power spectrum,

$$S_{\mathcal{J}}(f) = \int_{-\infty}^{\infty} dt C_0^{\mathcal{J}\mathcal{J}}(t) e^{2\pi \mathrm{i} f t} = \frac{a(\bar{\rho})}{L} \sum_q \frac{4f^2\pi^2\lambda_q}{a'^2\lambda_q^2 + 4f^2\pi^2}$$
$$\simeq a\left(\frac{\pi}{a'}\right)^{3/2} f^{3/2}, \tag{79}$$

a low-frequency far-from-critical beahvior $S_{\mathcal{J}}(f) \sim f^{\psi_J}$ with $\psi_J = 3/2$; for details, see Appendix F 3. On the other hand, near criticality, we obtain the low-frequency power spectrum $S_{\mathcal{J}}(f) \sim f^{\psi_{\mathcal{J}}}$, where

$$\psi_{\mathcal{J}} = 1 - \alpha, \tag{80}$$

by taking the Fourier transform of Eq. (77). Now, using the values of α in Eq. (74), we combine below the near- and far-from-critical values of the exponent $\psi_{\mathcal{J}}$ for the Oslo model,

$$\psi_{\mathcal{J}} \sim \begin{cases} (1 - \delta/\nu_\perp z) \simeq 0.803 & \text{for } \bar{\rho} \simeq \rho_c, \\ 3/2 & \text{for } \bar{\rho} \gg \rho_c. \end{cases} \tag{81}$$

We now compare simulations and the above theoretical predictions of the power spectrum. To this end, we discretize the instantaneous current into small temporal intervals, typically denoted as δt [48]. By using the Fourier transform $\tilde{\mathcal{J}}_{n;T} = \delta t \sum_{k=0}^{T-1} \mathcal{J}_i(k) e^{2\pi \mathrm{i} f_n k}$, the power spectrum of the bond current can be written as

$$S_{\mathcal{J}}(f_n) = \lim_{T\to\infty} \frac{1}{T} \langle |\tilde{\mathcal{J}}_{n;T}|^2 \rangle, \tag{82}$$

where $f_n = n/T$. In Fig. 11(a) we plot far-from-critical power spectrum $S_{\mathcal{J}}(f)$ vs frequency f for densities $\bar{\rho} = 2$ (red), 3 (blue), and 4 (green) in solid lines for $L = 1000$. The corresponding theoretical result, obtained by using Eq. (79) for $\bar{\rho} = 4.0$, is shown in the plot as a black dashed line. This asymptotic theoretical result quite nicely captures the $f^{3/2}$ decay of the power spectrum as $f \to 0$. In Fig. 11(b) we present the simulation data of the power spectrum for near-critical densities $\bar{\rho} = 1.7344$ (green line), 1.736 (blue line), and 1.738 (red line) for $L = 5000$. The upper guiding line, $f^{1-\alpha}$, is drawn following the relation $\psi_{\mathcal{J}} = 1 - \alpha$ as given in Eq. (80), where the near-critical value $\psi_{\mathcal{J}} \simeq 0.803$ is provided in Eq. (81). In the same figure, we also plot a lower guiding line, $f^{1/2}$, representing the normal decay of the power spectrum for a completely random diffusive system.

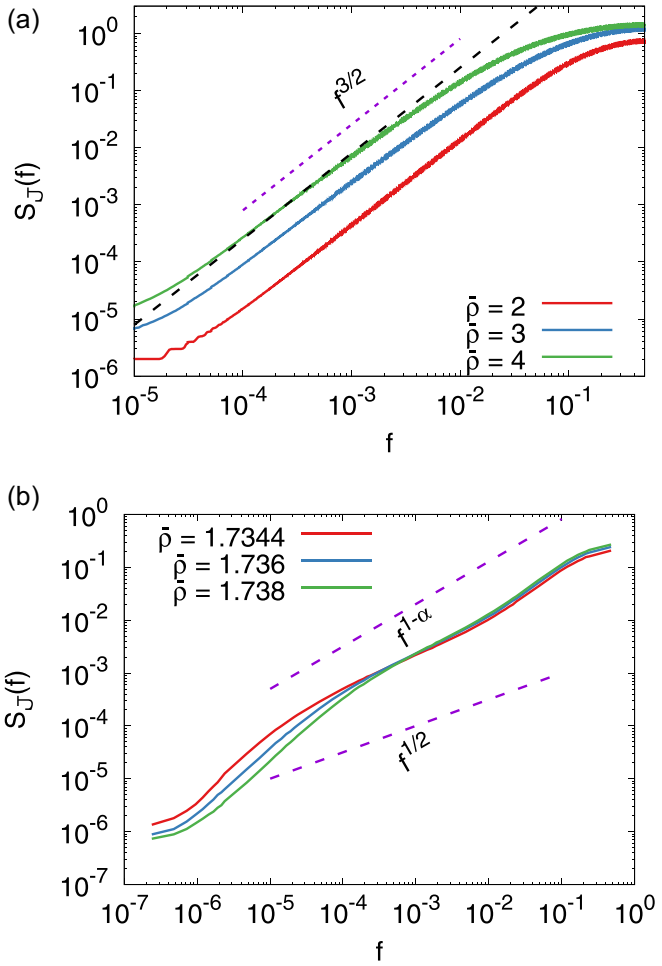

FIG. 11. Power spectra of the bond current vs frequency. (a) Far-from-critical power spectrum for bond current, for $L = 1000$, is plotted as solid lines for densities $\bar{\rho} = 2$ (red), $\bar{\rho} = 3$ (blue), and $\bar{\rho} = 4$ (green). Black-dotted asymptotic line is plotted using Eq. (79) for $\bar{\rho} = 4.0$ and nicely demonstrating the f^{ψ_J}, with $\psi_J = 3/2$ decay of the power spectrum as $f \to 0$. (b) This plot corresponds to the power spectrum of current to the density regime near criticality. Near-critical power spectrum for bond current, for $L = 5000$, is plotted for densities $\bar{\rho} = 1.738$ (red), 1.736 (blue), and 1.7344 (green). The $f^{1-\alpha}$ guiding line demonstrates theoretical prediction of the decay of the power spectrum near criticality, and the other guiding line represents $f^{1/2}$ (for the comparison with diffusive systems with single conservation law). The exponent $\psi_J = 1 - \alpha \simeq 0.803$ is obtained from Eq. (81).

6. *Power spectrum: Subsystem mass*

In this section we compute the power spectrum of subsystem mass by taking the Fourier transform of $C^{M_l M_l}(t)$ as given in Eq. (62):

$$\begin{aligned} S_M(f) &= \lim_{T\to\infty} \int_{-T}^{T} C^{M_l M_l}(t) e^{2\pi \mathbf{i} f t}\, dt \\ &= \frac{1}{L}\frac{a(\rho)}{2a'(\rho)} \sum_q \frac{2\lambda_q a'(\rho)}{\lambda_q^2 a'^2(\rho) + 4\pi^2 f^2} \lambda_{lq} \\ &\simeq \frac{a}{2\sqrt{\pi} a'^{3/2}} f^{-1/2}, \end{aligned} \tag{83}$$

where we approximate the sum as an integral for $L \gg 1$, $\lambda_{lq} \simeq 2$, and we use the transformation $x = \sqrt{f} y^{1/4}/\sqrt{2\pi a'}$. The asymptotic above behavior $S_M(f) \sim f^{-\psi_M}$, with $\psi_M = 1/2$, is consistent with the relation $\psi_M = 2 - \psi_J$, where the current power spectrum exponent $\psi_J = 3/2$. This relationship is a consequence of mass conservation and holds true both away from and near criticality. Thus, we obtain, using Eq. (80), the following scaling relation:

$$\psi_M = 1 + \alpha. \tag{84}$$

Using Eq. (81), we immediately combine the near- and far-from-critical values of the exponent ψ_M as

$$\psi_M = \begin{cases} (1 + \delta/\nu_\perp z) \simeq 1.197 & \text{for } \bar{\rho} \simeq \rho_c, \\ 1/2 & \text{for } \bar{\rho} \gg \rho_c, \end{cases} \tag{85}$$

where the value of the away from criticality exponent is the same as that we obtained in Eq. (83). That is, the power spectrum for subsystem mass in one dimension can be written as $S_M(f) \sim f^{-3/2+\mu}$. Evidently, positive $\mu > 0$ corresponds to an "anomalous" (more suppressed than that in diffusive systems having a single conservation law) fluctuation for subsystem mass; indeed, the anomalous fluctuation arises from "dynamic hyperuniformity" in the bond-current fluctuation. Also, for the Oslo model, we obtain, from Eq. (85), $\mu = 1/2 - \delta/\nu_\perp z$ near criticality and $\mu = 1$ away from criticality; these theoretical predictions are quite consistent with our estimates obtained in the previous section [see the text below Eq. (78)]. Interestingly, in Ref. [60] the authors studied a hard-sphere model of interacting particles undergoing active collisions with center-to-center impulsion (akin to a CoM or momentum conservation); the far-from-critical power spectrum for mass fluctuation was found to have a low-frequency $f^{-1/2}$ behavior and was explained from a phenomenological description of the modified Navier-Stokes equations. Notably, we also observe a similar behavior of the power spectrum in the Oslo model having similar conservation laws. However, in our microscopic dynamical theory [see Eq. (83)], this particular behavior has been explained from a different, and much simpler, description of diffusion [see Eq. (33)].

In Fig. 12(a) we plot a subsystem-mass power spectrum, which is obtained for subsystem size $l = 500$ and system size $L = 1000$ as a function of the frequency f, represented by solid lines, for density values away from the criticality: $\bar{\rho} = 2$ (red), 3 (blue), and 4 (green). The corresponding asymptotic line for $\bar{\rho} = 4.0$ is plotted in the black dotted line using Eq. (83). This asymptotic line demonstrates a nice agreement between the simulation and the $f^{-1/2}$ growth of the power spectrum as $f \to 0$ away from criticality. In Fig. 12(b) we present similar data, but for different subsystem and system sizes $l = 2500$ and $L = 5000$, respectively, for near-critical densities $\bar{\rho} = 1.7344$ (green line), 1.736 (blue line), and 1.738 (red line). The $f^{-(1+\alpha)}$ guiding line is drawn using Eq. (84), with $\psi_M \simeq 1.197$. The lower guiding line of $f^{-3/2}$, which is observed for diffusive systems having a single conserved quantity, is plotted for comparison purposes only.

V. STRUCTURE FACTOR

The static density fluctuation can also be quantified by the structure factor $S(q) = \langle |\delta\tilde{m}_q(t)|^2 \rangle / N$ [33], where $\delta\tilde{m}_q(t)$ is

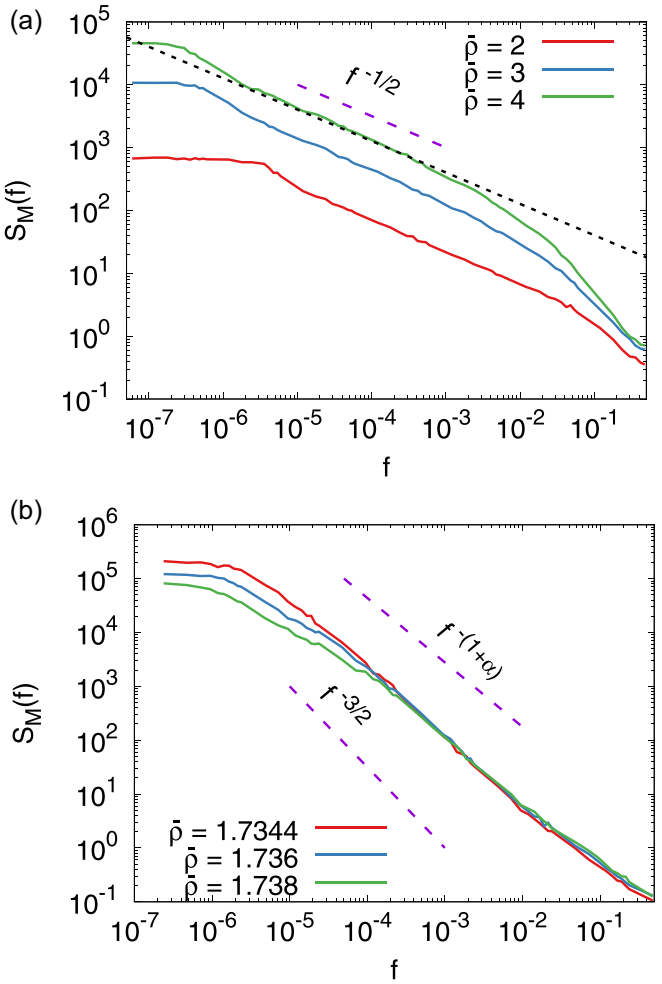

FIG. 12. Power spectra for subsystem mass vs frequency. (a) The power spectrum $S_M(f)$ obtained from simulations, for subsystem size $l = 500$ and system size $L = 1000$, are plotted as a function of frequency f for (far-from-critical) densities $\bar{\rho} = 2$ (red), 3 (blue), and 4 (green) as solid lines. The black dotted line corresponds to Eq. (83) for $\bar{\rho} = 4.0$, confirming that the far-from-critical subsystem-mass power spectrum varies as $f^{-1/2}$ in the small-frequency limit. (b) The power spectrum for subsystem mass, obtained from simulation for system size $L = 5000$ and subsystem size $l = 2500$, is plotted for near-critical density values $\bar{\rho} = 1.7344$ (green line), 1.736 (blue line), and 1.738 (red line). The guiding line representing $f^{-(1+\alpha)}$ is the near-critical asymptotic power spectrum for subsystem mass [obtained from theory, Eqs. (84) and (85)] as $f \to 0$, whereas the guiding line representing $f^{-3/2}$ for diffusive systems having a single conserved quantity is provided for comparison purposes.

the Fourier transform of the excess mass $\delta m_i(t) = m_i(t) - \bar{\rho}$ at a site i. For hyperuniform states, $S(q) \to 0$ as $q \to 0$; for the maximally hyperuniform states, $S(q) \sim q^2$ as $q \to 0$ [24]. We calculate $S(q)$ using the following microscopic evolution equation:

$$\frac{\partial}{\partial t}\delta m_i(t) = \left(\mathcal{J}^{(d)}_{i-1} - \mathcal{J}^{(d)}_{i}\right) + \left(\mathcal{J}^{(fl)}_{i-1} - \mathcal{J}^{(fl)}_{i}\right), \simeq D(\bar{\rho})\Delta_{i,k}\delta m_k(t) + \left(\mathcal{J}^{(fl)}_{i-1} - \mathcal{J}^{(fl)}_{i}\right). \quad (86)$$

First, we express $\delta m_i(t)$ and $\mathcal{J}^{(fl)}_i(t)$ in the Fourier modes and obtain

$$\frac{\partial}{\partial t}\delta\tilde{m}_q(t) \simeq -D\lambda_q\delta\tilde{m}_q(t) + (e^{\mathbf{i}q} - 1)\tilde{\mathcal{J}}^{(fl)}_q(t), \quad (87)$$

where $\tilde{\mathcal{J}}^{(fl)}_q(t)$ is the Fourier transform of $\mathcal{J}^{(fl)}$. We then solve the above equation to obtain

$$\delta\tilde{m}_q(t) = \int_0^t dt' e^{-\lambda_q D(t-t')}(e^{\mathbf{i}q} - 1)\tilde{\mathcal{J}}^{(fl)}_q(t') \quad (88)$$

and calculate the structure factor,

$$S(q) = \frac{1}{L\bar{\rho}}\langle|\delta\tilde{m}_q(t)|^2\rangle = \frac{1}{L\bar{\rho}}\int_0^t dt'\int_0^t dt'' e^{-\lambda_q D(t'-t'')}\lambda_q\left\langle\tilde{\mathcal{J}}^{(fl)}_q(t')\tilde{\mathcal{J}}^{(fl)}_{-q}(t'')\right\rangle. \quad (89)$$

Now, using Eq. (47), we write

$$\left\langle\tilde{\mathcal{J}}^{(fl)}_q(t')\tilde{\mathcal{J}}^{(fl)}_{q'}(t'')\right\rangle = La(\bar{\rho})\lambda_q\delta_{q,-q'}\delta(t'-t''), \quad (90)$$

and, by putting the above equation in Eq. (89), we obtain

$$S(q) = (1 - e^{-2\lambda_q Dt})\frac{\lambda_q}{2D\bar{\rho}}a(\bar{\rho}) \simeq \frac{a(\bar{\rho})}{2D\bar{\rho}}q^2, \quad (91)$$

where, in the last step, we take the limit $t \to \infty$ and approximate $\lambda(q) \simeq q^2$ for $q \to 0$. The above expression is valid far from criticality. In Fig. 13(a) we plot the structure factor obtained from simulations for $L = 2^{11}$, representing densities away from critical values: $\bar{\rho} = 2$ (red), $\bar{\rho} = 3$ (blue), and $\bar{\rho} = 4$ (green) shown as solid lines. Additionally, we plot our asymptotic expression in Eq. (91) as a black dotted line for $\bar{\rho} = 4$, demonstrating good agreement with the simulation data. The dotted magenta line represents the q^2 guiding line, denoting the functional dependence of the structure factor away from criticality on q. In Fig. 13(b) we plot the structure factor for densities near criticality: $\bar{\rho} = 1.734375$ for $L = 2^{14}$, and densities $\bar{\rho} = 1.736328125$ and 1.73828125 for $L = 2^{13}$. We also plot the guiding line $q^{0.5}$ in the dotted magenta line to signify the dependence of the structure factor on small q values near criticality. This dependence can be derived from the hyperuniform fluctuation of subsystem mass [see Eq. (68)].

VI. TAGGED PARTICLE DIFFUSION

In this section we examine the variance of the displacements $X_\alpha(T)$ of a tagged particle α in a temporal domain $[0, T]$. Since a particle can only hop a distance of $+1$ or -1 from the toppled site, the variance of the total hop length $\langle X^2_\alpha(T)\rangle$ depends solely on the number of topplings experienced by the tagged particle within this time interval, denoted as $N^{(h)}_\alpha(T)$, as shown in the following equation:

$$\langle X^2_\alpha(T)\rangle = N^{(h)}_\alpha(T). \quad (92)$$

By summing over all the tagged particles of the system, the total variance can be written in terms of twice of the total

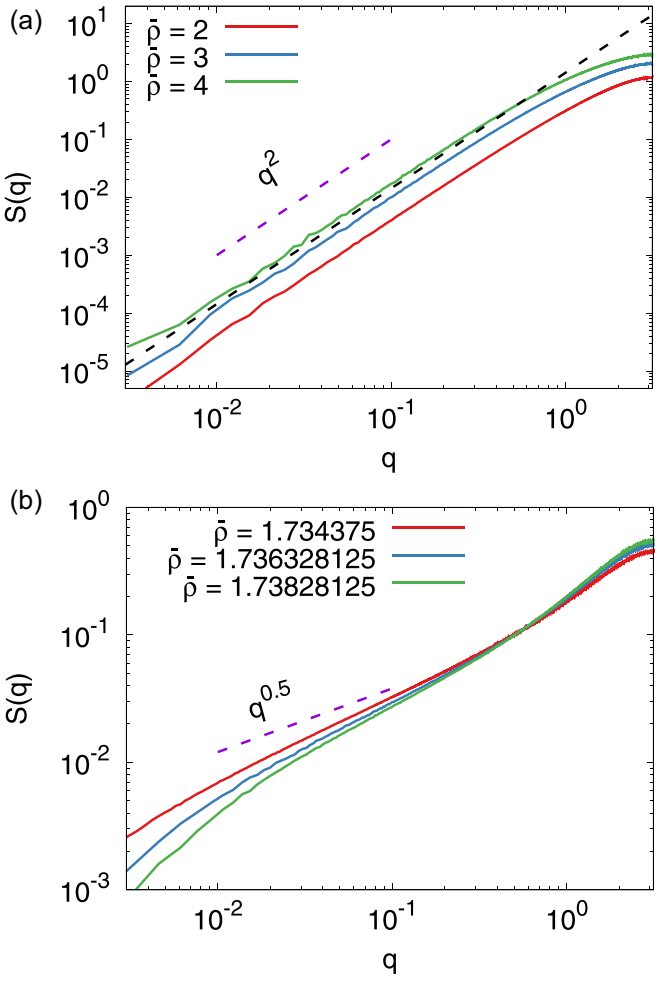

FIG. 13. (a) We plot static structure factor $S(q)$ for away from critical density values as a function of q for a system size of $L = 2^{11}$. We represent the simulation data with solid lines for density values of $\bar{\rho} = 2, 3$, and 4 from bottom to top. The dotted line corresponds to the theoretical asymptotic behavior of $S(q)$ for $\bar{\rho} = 4$ and is plotted using Eq. (91). (b) We plot static structure factor $S(q)$ for near-critical densities $\bar{\rho} = 1.734375$ (for $L = 2^{14}$), 1.736328125, 1.73828125 (for $L = 2^{13}$). The guiding line denotes the $q^{0.5}$ behavior of $S(q)$ for small wave numbers in the near-critical regime. The hyperuniform fluctuation of subsystem mass can also be used to capture this behavior [see Eq. (68)].

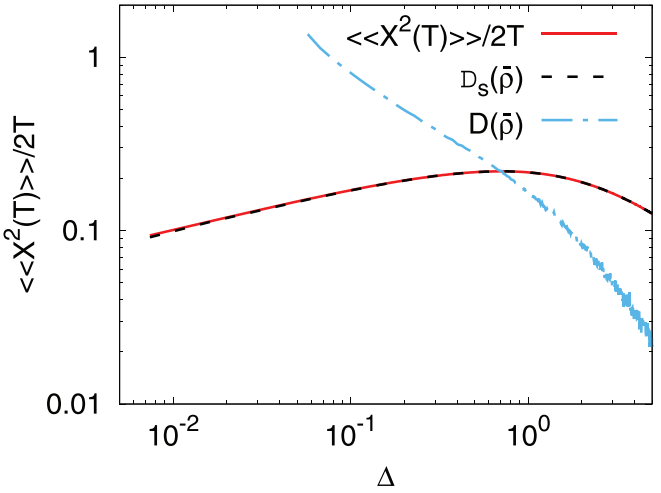

FIG. 14. Mean-square fluctuation of tagged particle displacement up to time T (solid red line) vs shifted density Δ, where double angular brackets $\langle\langle X^2(T)\rangle\rangle = \sum_\alpha \langle X_\alpha^2(T)\rangle/N$ imply average over both particles and trajectories. Simulations (solid red line) and the theoretically obtained self-diffusion coefficient $\mathcal{D}_s(\bar{\rho})$ (dashed black line) as in Eq. (96) provide a very good agreement. We also plot the bulk-diffusion coefficient $D(\bar{\rho}) = a'(\bar{\rho})$ vs $\Delta = \bar{\rho} - \rho_c$ (dot-dashed blue line), by calculating $D(\bar{\rho})$ through direct simulations where we use our theoretical result as in Eq. (7). Note that the bulk-diffusion coefficient and self-diffusion coefficient have qualitatively quite different behaviors.

topplings $N^{(tp)}(T)$ during that interval as

$$\sum_\alpha \langle X_\alpha^2(T)\rangle = \sum_\alpha N_\alpha^{(h)}(T) = 2N^{(tp)}(T), \tag{93}$$

as at each toppling two particles jump out of the site. The number of total topplings in the system, $N^{(tp)}(T)$, on average, is equal to the number of active site density $a(\bar{\rho})$ times the corresponding spacetime volume,

$$N^{(tp)}(T) = a(\bar{\rho})LT. \tag{94}$$

Due to the homogeneity of the system, we can express the left-hand side of Eq. (93) as the total number of particles multiplied by the variance of a particle tagged $\langle X^2(T)\rangle$. Using Eq. (94), we can rewrite Eq. (93) as $N\langle X^2(T)\rangle = 2a(\bar{\rho})LT$, or

$$\langle X^2(T)\rangle = 2\frac{a(\bar{\rho})}{\bar{\rho}}T \equiv 2\mathcal{D}_s(\bar{\rho})T, \tag{95}$$

leading to the exact expression of self-diffusion coefficient in terms of the activity and global density,

$$\mathcal{D}_s(\bar{\rho}) = \frac{a(\bar{\rho})}{\bar{\rho}}. \tag{96}$$

The mean square fluctuation of the cumulative displacement of the tagged particles up to time T (represented by the solid red line) is plotted in Fig. 14 as a function of the shifted density Δ. We denote double averaging over both trajectories and particles by $\langle\langle X^2(T)\rangle\rangle = \sum_\alpha \langle X_\alpha^2(T)\rangle/N$. We observe excellent congruence between the simulation data of $\langle\langle X^2(T)\rangle\rangle/2T$ (solid red line) and the self-diffusion coefficient $\mathcal{D}_s(\bar{\rho})$ obtained theoretically in Eq. (96) (shown as the dashed black line). Furthermore, to emphasize the contrasting behavior between the bulk- and self-diffusion coefficient, we display $D(\bar{\rho}) = a'(\bar{\rho})$ in the same figure (depicted by the dashed-dotted blue colored line), utilizing the relation in Eq. (7). Particularly near criticality, we observe that the activity and consequently the self-diffusion coefficient approach zero as the global density approaches its critical value. Meanwhile, the self-diffusion coefficient diverges, indicating anomalous transport. However, away from criticality, both coefficients tend towards zero in different manners, as depicted in the figure. We note that the self-diffusion coefficient for the conserved Manna sandpile satisfies a relationship similar to that given in Eq. (96).

VII. SUMMARY AND CONCLUSIONS

In this paper we use a microscopic approach for investigating the one-dimensional Oslo model on a ring geometry having L discrete sites. This model not only serves as a prototype for many-body systems with mass and CoM conservation, but it also has a broken time-reversal symmetry, resulting in the violation of detailed balance and a nonequilibrium phase transition. For the Oslo model, we provide a large-scale characterization of static and dynamic fluctuations of mass and current near as well as far from (above) criticality. We show that, despite having highly constrained microscopic dynamics due to CoM conservation, the Oslo model in fact exhibits *diffusive* relaxation far from criticality and *superdiffusive* relaxation near criticality. In the near-critical scaling regime, the relaxation time $\tau_r \sim L^z$ has an algebraic dependence on system size L, where the dynamical exponent $z = 2 - (1-\beta)/\nu_\perp < 2$ is determined by the two static exponents β and $\nu_\perp$. Indeed, the above scaling relation for the dynamic exponent predicted from our hydrodynamic theory is in perfect agreement with the "near-rational" values of the exponents obtained in Ref. [27] through large-scale simulations.

Quite interestingly, in the long-time limit, the additional CoM conservation manifests itself in making the temporal growth rate of time-integrated current fluctuation, and consequently the particle mobility, to *vanish.* Indeed, current fluctuations become anomalously suppressed as compared to those observed in diffusive systems with only mass conservation, leading to hyperuniformity in spatial as well as in temporal domains. To gain a theoretical understanding of the problem, we implement an approximate closure scheme, which helps one calculate unequal-time (two-point) correlation functions, and the associated power spectra, involving current and mass. We obtain a mass-conservation principle as encoded in Eq. (66), which connects (dynamic) current and (static) mass fluctuations and exactly determines the decay exponents of the respective dynamic correlation functions near criticality in terms of the standard static exponents. Far from criticality, we calculate the decay exponent exactly within the closure scheme. In this regime, we also calculate analytically the static structure factor, which has the behavior $S(q) \sim q^2$ in the limit of small wave number $q \to 0$ [see Eq. (91)]. Quite strikingly, far from criticality, the static structure factor exhibits "class I" hyperuniformity [34], whereas it exhibits "class III" hyperuniformity near (from above) criticality.

Notably, the dynamic properties of the Oslo model are qualitatively different from that observed in diffusive systems with a single conservation law, e.g., symmetric simple exclusion processes [59] and the conserved Manna sandpiles [48]. We provide a comparison between the Oslo model and the Manna sandpile (conserved-mass versions) in Table I to highlight the similarities and differences in the large-scale dynamic structure of the two models. Indeed, our findings reveal that, in the Oslo model, the bond-current correlation decays faster far from from criticality than it does near criticality. In other words, unlike diffusive systems with a single conserved quantity, fluctuations (static as well as dynamic) in the Oslo model are (anomalously) more suppressed far from criticality than near criticality. It is worth mentioning that the results obtained here are not specific to the Oslo model, but should be valid for a broad class of systems with both mass and CoM conservation.

TABLE I. A comparison between the conserved Oslo model and Manna sandpiles, concerning the steady-state dynamic properties, in terms of the following quantities: The variance of time-integrated bond-current $\mathcal{Q}_i(T)$ measured in time interval $[0, T]$, the power spectra $S_{\mathcal{J}}(f)$ and $S_M(f)$ of bond current and subsystem mass, respectively, and the three density-dependent transport coefficients: the bulk-diffusion coefficient $D(\bar{\rho})$, the mobility $\chi(\bar{\rho})$, and the self-diffusion coefficient $\mathcal{D}_s(\bar{\rho})$. The mobility $\chi = \lim_{T/L^2\to\infty, L\to\infty} L\langle \mathcal{Q}_i^2(T, L, \Delta)\rangle/T$ is defined by first taking the infinite-time limit ($T \to \infty$) and then the infinite-volume limit ($L \to \infty$).

Observables		Near criticality		Away from criticality	
$\langle \mathcal{Q}_i^2(T)\rangle_c$	$T^{\frac{1}{2}-\mu}$	Manna	Oslo	Manna	Oslo
$S_{\mathcal{J}}(f)$	$f^{\frac{1}{2}+\mu}$	$\mu = \frac{\beta+1}{2\nu_\perp z}$	$\mu = \frac{1-2\delta}{2\nu_\perp z}$	$\mu = 0$	$\mu = 1$
$S_M(f)$	$f^{-\frac{3}{2}+\mu}$				

Transport coefficients	Near criticality		Away from criticality	
	Manna	Olso	Manna	Oslo
χ	Δ^β	0	$2a$	0
D	$\Delta^{\beta-1}$	$\Delta^{\beta-1}$	$a'(\bar{\rho})$	$a'(\bar{\rho})$
$\mathcal{D}_s$	Δ^β	Δ^β	$a(\bar{\rho})/\bar{\rho}$	$a(\bar{\rho})/\bar{\rho}$

In conclusion, our analysis underscores the significance of conserved quantities in characterizing large-scale fluctuations in many-body systems. When compared to the other recently studied dynamically constrained systems, such as those with dipole-moment conservation [12,13,19], we have presented a prototypical CoM-conserving model, albeit with a contrasting (diffusive) relaxation mechanism, implying a far richer phenomenological structure in such systems than that anticipated earlier. Importantly, our findings demonstrate the crucial role of time-reversal symmetry (or the lack of it) in determining the large-scale (hydrodynamic) properties of a CoM-conserving system. We believe they will shed light on the dynamical origin of hyperuniform fluctuations in systems with multiple conservation laws, as well as provide a fresh perspective on the general theoretical understanding of the problem.

ACKNOWLEDGMENTS

We thank Deepak Dhar, S. S. Manna, and Salvatore Torquato for very helpful discussions and for careful reading of the manuscript.

APPENDIX A: UNEQUAL-TIME MASS AND INTEGRATED CURRENT CORRELATION FUNCTION

Here we present the derivation of Eq. (36) using the following microscopic update rules of the quantity

$m_i(t+dt)\mathcal{Q}_{i+r}(t')$ for $t > t'$:

$$m_i(t+dt)\mathcal{Q}_{i+r}(t') = \begin{cases} \text{events} & \text{probabilities} \\ (m_i(t)+1)\mathcal{Q}_{i+r}(t') & (\hat{a}_{i+1}+\hat{a}_{i-1})dt \\ (m_i(t)-2)\mathcal{Q}_{i+r}(t') & \hat{a}_i dt \\ m_i(t)\mathcal{Q}_{i+r}(t') & (1-\Sigma dt), \end{cases} \tag{A1}$$

where the probability of nothing happening in the interval dt is $1-\Sigma dt$, we obtain the corresponding evolution equation for $C_r^{m\mathcal{Q}}(t,t')$ as

$$\frac{d}{dt}C_r^{m\mathcal{Q}}(t,t') = \sum_k \Delta_{i,k}\langle \hat{a}_k(t)\mathcal{Q}_{i+r}(t')\rangle = \left\langle \left\{\mathcal{J}_{i-1}^{(d)}(t) - \mathcal{J}_i^{(d)}(t)\right\}\mathcal{Q}_{i+r}(t')\right\rangle, \tag{A2}$$

where $\Delta_{i,k} = (\delta_{i+1,k} + \delta_{i-1,k} - 2\delta_{i,k})$ is the discrete Laplacian operator. We further simplify the above equation by approximating the diffusive current by Eq. (33) and obtain the following equation:

$$\frac{d}{dt}C_r^{m\mathcal{Q}}(t,t') \simeq a'(\bar{\rho})\sum_k \Delta_{i,k}\langle m_k(t)\mathcal{Q}_{i+r}(t')\rangle. \tag{A3}$$

We can write the solution of the above equation using the discrete Fourier transformation [defined in Eq. (28)] as

$$\tilde{C}_q^{m\mathcal{Q}}(t,t') = \exp[-a'(\bar{\rho})\lambda_q(t-t')]\tilde{C}_q^{m\mathcal{Q}}(t',t'), \tag{A4}$$

where $\tilde{C}_q^{m\mathcal{Q}}(t,t')$ is the Fourier transformed $C_r^{m\mathcal{Q}}(t,t')$ and $\lambda_q = 2[1-\cos q]$ are the eigenvalues of the discrete Laplacian.

APPENDIX B: EQUAL-TIME MASS AND INTEGRATED CURRENT CORRELATION FUNCTION

The expression of Eq. (36) also requires the and equal-time mass and integrated current correlation function. Using the update rules,

$$m_i(t+dt)\mathcal{Q}_{i+r}(t+dt) = \begin{cases} \text{events} & \text{probabilities} \\ (m_i(t)+1)(\mathcal{Q}_{i+r}(t)+1) & \hat{a}_{i+1}\delta_{i+r,i+1}dt \\ (m_i(t)+1)(\mathcal{Q}_{i+r}(t)-1) & \hat{a}_{i+1}\delta_{i+r,i}dt \\ (m_i(t)+1)(\mathcal{Q}_{i+r}(t)+1) & \hat{a}_{i-1}\delta_{i+r,i-1}dt \\ (m_i(t)+1)(\mathcal{Q}_{i+r}(t)-1) & \hat{a}_{i-1}\delta_{i+r,i-2}dt \\ (m_i(t)-2)(\mathcal{Q}_{i+r}(t)+1) & \hat{a}_i\delta_{i+r,i}dt \\ (m_i(t)-2)(\mathcal{Q}_{i+r}(t)-1) & \hat{a}_i\delta_{i+r,i-1}dt \\ (m_i(t)+1)\mathcal{Q}_{i+r}(t) & \hat{a}_{i+1}(1-\delta_{i+r,i+1}-\delta_{i+r,i})dt \\ (m_i(t)+1)\mathcal{Q}_{i+r}(t) & \hat{a}_{i-1}(1-\delta_{i+r,i-1}-\delta_{i+r,i-2})dt \\ (m_i(t)-2)\mathcal{Q}_{i+r}(t) & \hat{a}_i(1-\delta_{i+r,i}-\delta_{i+r,i-1})dt \\ m_i(t)(\mathcal{Q}_{i+r}(t)+1) & \hat{a}_{i+r} \\ & (1-\delta_{i+r,i}-\delta_{i+r+1,i}-\delta_{i+r-1,i})dt \\ m_i(t)(\mathcal{Q}_{i+r}(t)-1) & \hat{a}_{i+r+1} \\ & (1-\delta_{i+r,i}-\delta_{i+r+1,i}-\delta_{i+r+2,i})dt \\ m_i(t)\mathcal{Q}_{i+r}(t) & 1-\Sigma dt, \end{cases} \tag{B1}$$

where the probability of nothing happening in the interval dt is $1-\Sigma dt$, we obtain the evolution equation of the correlation of equal-time mass and current,

$$\frac{d}{dt}\langle m_i(t)\mathcal{Q}_{i+r}(t)\rangle = \sum_k \Delta_{i,k}\langle \hat{a}_k(t)\mathcal{Q}_{i+r}(t)\rangle + f_{i,r}(t) \simeq a'\sum_k \Delta_{i,k}\langle m_k(t)\mathcal{Q}_{i+r}(t)\rangle + f_{i,r}(t), \tag{B2}$$

where we used the approximation (33); the source term $f_{i,r}(t)$ has the following representation:

$$f_{i,r}(t) = \langle m_i(t)\hat{a}_{i+r}(t)\rangle - \langle m_i(t)\hat{a}_{i+r+1}(t)\rangle + \langle \hat{a}_{i+1}\rangle(\delta_{i+r,i+1}-\delta_{i+r,i}) + \langle \hat{a}_{i-1}\rangle(\delta_{i+r,i-1}-\delta_{i+r,i-2}) - 2\langle \hat{a}_i\rangle(\delta_{i+r,i}-\delta_{i+r,i-1}), \tag{B3}$$

and in the steady state, it will simply be

$$f_r = C_r^{m\hat{a}} - C_{r+1}^{m\hat{a}} + a\{3(\delta_{0,r+1}-\delta_{0,r}) + (\delta_{0,r-1}-\delta_{0,r+2})\}, \tag{B4}$$

where $C_r^{m\hat{a}}$ is the equal-time mass and activity correlation function in the steady state. We obtain Eq. (37) by solving Eq. (B2) in Fourier mode, and Eq. (38) is the Fourier representation of Eq. (B4). In the following section, we derive the steady-state correlation function $C_r^{m\hat{a}}$.

APPENDIX C: EQUAL-TIME MASS-ACTIVITY CORRELATION

To obtain Eq. (39), we write the evolution equation of the equal-time and unequal space mass-mass correlation function using the following update rules:

$$m_i(t+dt)m_{i+r}(t+dt) = \begin{cases} \text{events} & \text{probabilities} \\ (m_i(t)-2)(m_{i+r}(t)-2) & \hat{a}_i\delta_{i,i+r}dt \\ (m_i(t)-2)(m_{i+r}(t)+1) & \hat{a}_i\delta_{i+1,i+r}dt \\ (m_i(t)-2)(m_{i+r}(t)+1) & \hat{a}_i\delta_{i-1,i+r}dt \\ (m_i(t)+1)(m_{i+r}(t)+1) & \hat{a}_{i-1}\delta_{i,i+r}dt \\ (m_i(t)+1)(m_{i+r}(t)-2) & \hat{a}_{i-1}\delta_{i-1,i+r}dt \\ (m_i(t)+1)(m_{i+r}(t)+1) & \hat{a}_{i-1}\delta_{i-2,i+r}dt \\ (m_i(t)+1)(m_{i+r}(t)+1) & \hat{a}_{i+1}\delta_{i,i+r}dt \\ (m_i(t)+1)(m_{i+r}(t)-2) & \hat{a}_{i+1}\delta_{i+1,i+r}dt \\ (m_i(t)+1)(m_{i+r}(t)+1) & \hat{a}_{i+1}\delta_{i+2,i+r}dt \\ (m_i(t)-2)m_{i+r}(t) & \hat{a}_i(1-\delta_{i+1,i+r}-\delta_{i,i+r}-\delta_{i-1,i+r})dt \\ (m_i(t)+1)m_{i+r}(t) & \hat{a}_{i-1}(1-\delta_{i-1,i+r}-\delta_{i,i+r}-\delta_{i-2,i+r})dt \\ (m_i(t)+1)m_{i+r}(t) & \hat{a}_{i+1}(1-\delta_{i+1,i+r}-\delta_{i,i+r}-\delta_{i+2,i+r})dt \\ m_i(t)(m_{i+r}(t)-2) & \hat{a}_{i+r}(1-\delta_{i,i+r+1}-\delta_{i,i+r}-\delta_{i,i+r-1})dt \\ m_i(t)(m_{i+r}(t)+1) & \hat{a}_{i+r+1}(1-\delta_{i,i+r+1}-\delta_{i,i+r+2}-\delta_{i,i+r})dt \\ m_i(t)(m_{i+r}(t)+1) & \hat{a}_{i+r-1}(1-\delta_{i,i+r-1}-\delta_{i,i+r}-\delta_{i,i+r-2})dt \\ m_i(t)m_{i+r}(t) & 1-\Sigma dt, \end{cases} \tag{C1}$$

where the probability of nothing happening in the interval dt is $1-\Sigma dt$. The corresponding evolution equation of $C_r^{mm}(t,t)$ can be written using the above update rules as

$$\frac{d}{dt}C_r^{mm}(t,t) = \sum_k \Delta_{i,k}\langle \hat{a}_k m_{i+r}\rangle + \sum_k \Delta_{i+r,k}\langle m_i \hat{a}_k\rangle + B_{i,i+r}, \tag{C2}$$

where $B_{i,i+r}$ is the source part of this correlation, given as

$$B_{i,i+r} = \delta_{i,i+r}(4a_i + a_{i-1} + a_{i+1}) - 2\delta_{i-1,i+r}(a_i + a_{i-1}) - 2\delta_{i+1,i+r}(a_i + a_{i+1}) + \delta_{i-2,i+r}a_{i-1} + \delta_{i+2,i+r}a_{i+1}. \tag{C3}$$

In the steady state we must have $\frac{d}{dt}C_r^{mm}(t,t) = 0$, and using the translation symmetry, Eq. (C2) can be written as

$$2\left(C_{r-1}^{\hat{a}m} - C_r^{\hat{a}m} + C_{r+1}^{\hat{a}m}\right) + B_r = 0, \tag{C4}$$

and the source term B_r is given by

$$B_r = 6a(\bar{\rho})\delta_{0,r} - 4a(\bar{\rho})(\delta_{0,r+1} + \delta_{0,r-1}) + a(\bar{\rho})(\delta_{0,r+2} + \delta_{0,r-2}). \tag{C5}$$

Note that we can also straightforwardly derive Eq. (56) simply by inserting our truncation relation, as given in Eq. (33), into Eq. (C4). We can solve Eq. (C4) by multiplying both sides by z^r and defining the generating function $G(z) = \sum_{r=0}^{\infty} z^r C_r^{\hat{a}m}$. Imposing the convergence of $G(z) < \infty$ when $z \to 1$, we can write the generating function as

$$G(z) = a(\bar{\rho}) - \frac{a(\bar{\rho})}{2}z. \tag{C6}$$

From the generating function of above, we write the correlation $C_r^{\hat{a}m}$, in steady state, as

$$C_r^{\hat{a}m} = a(\bar{\rho})\delta_{0,r} - \frac{a(\bar{\rho})}{2}(\delta_{r+1} + \delta_{r-1}), \tag{C7}$$

and thus we obtain Eq. (39).

APPENDIX D: EQUAL-TIME CURRENT-CURRENT CORRELATION

To derive Eq. (42), we write the evolution equation of the equal-time unequal-space correlation of the time-integrated bond current using the following update equation:

$$\mathcal{Q}_i(t+dt)\mathcal{Q}_{i+r}(t+dt) = \begin{cases} \text{events} & \text{probabilities} \\ (\mathcal{Q}_i(t)+1)(\mathcal{Q}_{i+r}(t)+1) & \hat{a}_i(t)\delta_{i,i+r}dt \\ (\mathcal{Q}_i(t)+1)(\mathcal{Q}_{i+r}(t)-1) & \hat{a}_i(t)\delta_{i-1,i+r}dt \\ (\mathcal{Q}_i(t)-1)(\mathcal{Q}_{i+r}(t)-1) & \hat{a}_{i+1}(t)\delta_{i,i+r}dt \\ (\mathcal{Q}_i(t)-1)(\mathcal{Q}_{i+r}(t)+1) & \hat{a}_{i+1}(t)\delta_{i+1,i+r}dt \\ (\mathcal{Q}_i(t)+1)\mathcal{Q}_{i+r}(t) & \hat{a}_i(t)(1-\delta_{i,i+r}-\delta_{i-1,i+r})dt \\ (\mathcal{Q}_i(t)-1)\mathcal{Q}_{i+r}(t) & \hat{a}_{i+1}(t)(1-\delta_{i,i+r}-\delta_{i+1,i+r})dt \\ \mathcal{Q}_i(t)(\mathcal{Q}_{i+r}(t)+1) & \hat{a}_{i+r}(t)(1-\delta_{i,i+r}-\delta_{i,i+r-1})dt \\ \mathcal{Q}_i(t)(\mathcal{Q}_{i+r}(t)-1) & \hat{a}_{i+r+1}(t)(1-\delta_{i,i+r}-\delta_{i,i+r+1})dt \\ \mathcal{Q}_i(t)\mathcal{Q}_{i+r}(t) & 1-\Sigma dt, \end{cases} \tag{D1}$$

where $1-\Sigma dt$ is the probability of nothing happening in the time interval dt. The corresponding dynamical equation can be written as

$$\frac{\partial}{\partial t}C_r^{\mathcal{Q}\mathcal{Q}}(t,t) = \Gamma_{i,i+r}(t) + \left\langle \mathcal{J}_i^{(d)}(t)\mathcal{Q}_{i+r}(t)\right\rangle_c + \left\langle \mathcal{Q}_i(t)\mathcal{J}_{i+r}^{(d)})(t)\right\rangle_c, \tag{D2}$$

where $\Gamma_{i,i+r}$ is the source of the correlation, which can be written as

$$\Gamma_{i,i+r}(t) = a_i(t)(\delta_{i,i+r}-\delta_{i-1,i+r}) - a_{i+1}(t)(\delta_{i+1,i+r}-\delta_{i,i+r}). \tag{D3}$$

In the steady state, the above source becomes

$$\Gamma_r(t) = a(\bar{\rho})(2\delta_{0,r}-\delta_{0,r+1}-\delta_{0,r-1}). \tag{D4}$$

Equation (D2) and Eq. (D4), respectively, explain Eq. (42) and Eq. (45).

APPENDIX E: UNEQUAL-TIME SPATIAL MASS CORRELATION FUNCTION

The derivation of Eq. (55) requires the dynamical equation satisfied by the unequal-time spatial correlation of mass, $C_r^{mm}(t)$, which is given by

$$\frac{d}{dt}C_r^{mm}(t) = \sum_k \Delta_{i,k}\langle \hat{a}_k(t)m_{i+r}(0)\rangle. \tag{E1}$$

The above equation can be derived using the following update rules for $t > t'$:

$$m_i(t+dt)m_{i+r}(t') = \begin{cases} \text{events} & \text{probabilities} \\ (m_i(t)+1)m_{i+r}(t') & \hat{a}_{i+1}dt \\ (m_i(t)+1)m_{i+r}(t') & \hat{a}_{i-1}dt \\ (m_i(t)-2)m_{i+r}(t') & \hat{a}_i dt \\ m_i(t)m_{i+r}(t') & 1-\Sigma dt, \end{cases} \tag{E2}$$

where $1-\Sigma dt$ is the probability of nothing happening in the interval dt. Equation (E1) can be simplified further using the approximation scheme given in Eq. (33) as

$$\frac{d}{dt}C_r^{mm}(t) \simeq a'\sum_k \Delta_{r,k}C_k^{mm}(t). \tag{E3}$$

Equation (55) is simply the solution of the above equation in the Fourier domain.

APPENDIX F: ASYMPTOTIC ANALYSIS

1. Equal-time current correlation

In this section we derive the asymptotic expression of Eq. (52), which, by rearranging the sum, can be rewritten as

$$\left\langle \mathcal{Q}_i^2(T)\right\rangle = \frac{a}{a'} - \frac{a}{a'}\frac{1}{L}\sum_q e^{-a'\lambda_q T} + O\left(\frac{1}{L}\right), \tag{F1}$$

where we have used $\sum_q 1/L \simeq 1$. Now going to the continuum limit, we have

$$\left\langle \mathcal{Q}_i^2(T)\right\rangle \simeq \frac{a}{a'} - 2\frac{a}{a'}\int_{1/L}^{1/2} e^{-a'\lambda(x)T}dx, \tag{F2}$$

where $\lambda(x) \simeq 4\pi^2x^2$. Furthermore, using the variable transformation $z = 4\pi^2x^2a'T$, the above expression can be simplified as

$$\left\langle \mathcal{Q}_i^2(T)\right\rangle \simeq \frac{a}{a'} - \frac{aT^{-1/2}}{2\pi a'^{\frac{3}{2}}}\int_0^\infty dz\frac{e^{-z}}{\sqrt{z}} = \frac{a}{a'} - \frac{aT^{-1/2}}{2\sqrt{\pi}a'^{\frac{3}{2}}}, \tag{F3}$$

in the limit $T \gg 1$ being large.

2. Dynamic correlation of bond current

The decay of the bond current correlation over time is governed by the second part of the right-hand side of Eq. (75). Its asymptotic for $t \gg 1$ and for a single bond $r = 0$ can be understood by converting the sum into an integral in the continuum limit using $i \to x = i/L$, where λ_q can be approximated as $\lambda_q \to \lambda(x) \simeq 4\pi^2x^2$. Then, using the variable transformation $z = 4\pi^2x^2a't$, we can write Eq. (75) for $t \gg 1$ as follows:

$$C_0^{\mathcal{J}\mathcal{J}}(t) \simeq -\frac{at^{-5/2}}{4\pi a'^{3/2}}\int_0^\infty e^{-z}z^{3/2}dz = -\frac{3at^{-5/2}}{16\sqrt{\pi}a'^{3/2}}. \tag{F4}$$

The above equation appeared in Eq. (76).

3. Power spectrum of bond current

In the limit of the large system size, $L \gg 1$, the power spectrum of the bond current, expressed as an exact sum in the first line of Eq. (79), in the frequency domain $1/L^2 \ll f \ll 1$, can be approximated as an integral,

$$S_{\mathcal{J}}(f) \simeq 2a \int_{\frac{1}{L}}^{\frac{1}{2}} dx \lambda(x) \frac{4\pi^2 f^2}{\lambda(x)^2 a'^2 + 4\pi^2 f^2}, \tag{F5}$$

where in the continuum limit, we perform the substitution $q = 2\pi x$, which leads to $\lambda(x) \approx 4\pi^2 x^2$. Then using the variable transformation, $x = \sqrt{f} y^{1/4}/\sqrt{2\pi a'}$, we convert the above integral into the following in the limit $L \to \infty$ and obtain the following:

$$S_{\mathcal{J}}(f) = f^{3/2} \frac{a\sqrt{\pi}}{\sqrt{2} a'^{3/2}} \int_0^\infty \frac{dy}{y^{1/4}(1+y)} = a \frac{\pi^{3/2}}{a'^{3/2}} f^{3/2}. \tag{F6}$$

Thus, we derive the asymptotic expression of the power spectrum of the bond current, which appeared in the second line of Eq. (79).

[1] L. Vidmar and M. Rigol, Generalized Gibbs ensemble in integrable lattice models, J. Stat. Mech.: Theory Exp. (2016) 064007.

[2] H. Spohn, *Hydrodynamic Scales of Integrable Many-Body Systems* (World Scientific, Singapore, 2023).

[3] C. Boldrighini, R. L. Dobrushin, and Y. M. Sukhov, One-dimensional hard rod caricature of hydrodynamics, J. Stat. Phys. **31**, 577 (1983).

[4] H. Spohn, Generalized Gibbs ensembles of the classical Toda chain, J. Stat. Phys. **180**, 4 (2020).

[5] O. A. Castro-Alvaredo, B. Doyon, and T. Yoshimura, Emergent hydrodynamics in integrable quantum systems out of equilibrium, Phys. Rev. X **6**, 041065 (2016).

[6] H. Spohn, Hydrodynamic equations for the Ablowitz–Ladik discretization of the nonlinear Schrödinger equation, J. Math. Phys. **63**, 033305 (2022).

[7] H. Spohn, *Large Scale Dynamics of Interacting Particles* (Springer, Berlin, 2012).

[8] C. Kipnis and C. Landim, *Scaling Limits of Interacting Particle Systems*, Grundlehren der mathematischen Wissenschaften (Springer, Berlin, Heidelberg, 1999).

[9] L. Bertini, A. De Sole, D. Gabrielli, G. Jona-Lasinio, and C. Landim, Macroscopic fluctuation theory, Rev. Mod. Phys. **87**, 593 (2015).

[10] A. Prem, M. Pretko, and R. M. Nandkishore, Emergent phases of fractonic matter, Phys. Rev. B **97**, 085116 (2018).

[11] A. Gromov, A. Lucas, and R. M. Nandkishore, Fracton hydrodynamics, Phys. Rev. Res. **2**, 033124 (2020).

[12] J. Feldmeier, P. Sala, G. De Tomasi, F. Pollmann, and M. Knap, Anomalous diffusion in dipole- and higher-moment-conserving systems, Phys. Rev. Lett. **125**, 245303 (2020).

[13] A. Morningstar, V. Khemani, and D. A. Huse, Kinetically constrained freezing transition in a dipole-conserving system, Phys. Rev. B **101**, 214205 (2020).

[14] P. Sala, T. Rakovszky, R. Verresen, M. Knap, and F. Pollmann, Ergodicity breaking arising from Hilbert space fragmentation in dipole-conserving Hamiltonians, Phys. Rev. X **10**, 011047 (2020).

[15] S. Pai, M. Pretko, and R. M. Nandkishore, Localization in fractonic random circuits, Phys. Rev. X **9**, 021003 (2019).

[16] P. Glorioso, J. Guo, J. F. Rodriguez-Nieva, and A. Lucas, Breakdown of hydrodynamics below four dimensions in a fracton fluid, Nat. Phys. **18**, 912 (2022).

[17] S. Scherg, T. Kohlert, P. Sala, F. Pollmann, B. Hebbe Madhusudhana, I. Bloch, and M. Aidelsburger, Observing non-ergodicity due to kinetic constraints in tilted Fermi-Hubbard chains, Nat. Commun. **12**, 4490 (2021).

[18] V. B. Shenoy and R. Moessner, (k, n)-fractonic Maxwell theory, Phys. Rev. B **101**, 085106 (2020).

[19] J. H. Han, E. Lake, and S. Ro, Scaling and Localization in multipole-conserving diffusion, Phys. Rev. Lett. **132**, 137102 (2024).

[20] T. Bertrand, D. Chatenay, and R. Voituriez, Nonlinear diffusion and hyperuniformity from Poisson representation in systems with interaction mediated dynamics, New J. Phys. **21**, 123048 (2019).

[21] L. Corté, P. M. Chaikin, J. P. Gollub, and D. J. Pine, Random organization in periodically driven systems, Nat. Phys. **4**, 420 (2008).

[22] Q.-L. Lei, M. P. Ciamarra, and R. Ni, Nonequilibrium strongly hyperuniform fluids of circle active particles with large local density fluctuations, Sci. Adv. **5**, eaau7423 (2019).

[23] Y. Kuroda and K. Miyazaki, Microscopic theory for hyperuniformity in two-dimensional chiral active fluid, J. Stat. Mech.: Theory Exp. (2023) 103203.

[24] D. Hexner and D. Levine, Noise, diffusion, and hyperuniformity, Phys. Rev. Lett. **118**, 020601 (2017).

[25] H. Ikeda, Harmonic chain far from equilibrium: Single-file diffusion, long-range order, and hyperuniformity, arXiv:2309.03155 (2023).

[26] K. Christensen, Á. Corral, V. Frette, J. Feder, and T. Jøssang, Tracer dispersion in a self-organized critical system, Phys. Rev. Lett. **77**, 107 (1996).

[27] P. Grassberger, D. Dhar, and P. K. Mohanty, Oslo model, hyperuniformity, and the quenched Edwards-Wilkinson model, Phys. Rev. E **94**, 042314 (2016).

[28] R. Dickman and S. D. da Cunha, Particle-density fluctuations and universality in the conserved stochastic sandpile, Phys. Rev. E **92**, 020104(R) (2015).

[29] S. Lübeck, Universal scaling behavior of non-equilibrium phase transitions, Int. J. Mod. Phys. B **18**, 3977 (2004).

[30] R. Dickman, M. A. Muñoz, A. Vespignani, and S. Zapperi, Paths to self-organized criticality, Braz. J. Phys. **30**, 27 (2000).

[31] S. Torquato and F. H. Stillinger, Local density fluctuations, hyperuniformity, and order metrics, Phys. Rev. E **68**, 041113 (2003).

[32] S. Torquato, Hyperuniformity and its generalizations, Phys. Rev. E **94**, 022122 (2016).

[33] S. Torquato, Hyperuniform states of matter, Phys. Rep. **745**, 1 (2018).

[34] S. Torquato, Diffusion spreadability as a probe of the microstructure of complex media across length scales, Phys. Rev. E **104**, 054102 (2021).
[35] D. J. Pine, J. P. Gollub, J. F. Brady, and A. M. Leshansky, Chaos and threshold for irreversibility in sheared suspensions, Nature (London) **438**, 997 (2005).
[36] R. Jeanneret and D. Bartolo, Geometrically protected reversibility in hydrodynamic Loschmidt-echo experiments, Nat. Commun. **5**, 3474 (2014).
[37] D. Hexner and D. Levine, Hyperuniformity of critical absorbing states, Phys. Rev. Lett. **114**, 110602 (2015).
[38] J. H. Weijs, R. Jeanneret, R. Dreyfus, and D. Bartolo, Emergent hyperuniformity in periodically driven emulsions, Phys. Rev. Lett. **115**, 108301 (2015).
[39] R. Garcia-Millan, G. Pruessner, L. Pickering, and K. Christensen, Correlations and hyperuniformity in the avalanche size of the Oslo model, Europhys. Lett. **122**, 50003 (2018).
[40] J. Kertesz and L. B. Kiss, The noise spectrum in the model of self-organised criticality, J. Phys. A: Math. Gen. **23**, L433 (1990).
[41] S. S. Manna and J. Kertész, Correlations and scaling in the outflow statistics of a sandpile automaton, Physica A **173**, 49 (1991).
[42] L. Laurson, M. J. Alava, and S. Zapperi, Power spectra of self-organized critical sandpiles, J. Stat. Mech.: Theory Exp. (2005) L11001.
[43] J. M. Carlson, J. T. Chayes, E. R. Grannan, and G. H. Swindle, Self-orgainzed criticality and singular diffusion, Phys. Rev. Lett. **65**, 2547 (1990).
[44] S. D. da Cunha, R. R. Vidigal, L. R. da Silva, and R. Dickman, Diffusion in stochastic sandpiles, Eur. Phys. J. B **72**, 441 (2009).
[45] A. C. Yadav, R. Ramaswamy, and D. Dhar, Power spectrum of mass and activity fluctuations in a sandpile, Phys. Rev. E **85**, 061114 (2012).
[46] S. Chatterjee, A. Das, and P. Pradhan, Hydrodynamics, density fluctuations, and universality in conserved stochastic sandpiles, Phys. Rev. E **97**, 062142 (2018).
[47] D. Tapader, P. Pradhan, and D. Dhar, Density relaxation in conserved Manna sandpiles, Phys. Rev. E **103**, 032122 (2021).
[48] A. Mukherjee and P. Pradhan, Dynamic correlations in the conserved Manna sandpile, Phys. Rev. E **107**, 024109 (2023).
[49] P. Le Doussal and K. J. Wiese, Exact mapping of the stochastic field theory for Manna sandpiles to interfaces in random media, Phys. Rev. Lett. **114**, 110601 (2015).
[50] A. Shapira and K. J. Wiese, Anchored advected interfaces, Oslo model, and roughness at depinning, J. Stat. Mech.: Theory Exp. (2023) 063202.
[51] P. Bak, *How Nature Works: The Science of Self-organized Criticality* (Oxford University Press, Oxford, 1997).
[52] D. Dhar, Self-organized critical state of sandpile automaton models, Phys. Rev. Lett. **64**, 1613 (1990).
[53] D. Dhar, The Abelian sandpile and related models, Physica A **263**, 4 (1999).
[54] S. S. Manna, Two-state model of self-organized criticality, J. Phys. A: Math. Gen. **24**, L363 (1991).
[55] R. Dickman, M. Alava, M. A. Muñoz, J. Peltola, A. Vespignani, and S. Zapperi, Critical behavior of a one-dimensional fixed-energy stochastic sandpile, Phys. Rev. E **64**, 056104 (2001).
[56] P. K. Mohanty and D. Dhar, Generic sandpile models have directed percolation exponents, Phys. Rev. Lett. **89**, 104303 (2002).
[57] P. K. Mohanty and D. Dhar, Critical behavior of sandpile models with sticky grains, Physica A **384**, 34 (2007).
[58] L. P. Kadanoff, S. R. Nagel, L. Wu, and S.-M. Zhou, Scaling and universality in avalanches, Phys. Rev. A **39**, 6524 (1989).
[59] T. Sadhu and B. Derrida, Correlations of the density and of the current in non-equilibrium diffusive systems, J. Stat. Mech.: Theory Exp. (2016) 113202.
[60] Q.-L. Lei and R. Ni, Hydrodynamics of random-organizing hyperuniform fluids, Proc. Natl. Acad. Sci. USA **116**, 22983 (2019).